INFORMATION TO USERS

This manuscript has been reproduced from the microfilm master. UMI films the text directly from the original or copy submitted. Thus, some thesis and dissertation copies are in typewriter face, while others may be from any type of computer printer.

The quality of this reproduction is dependent upon the quality of the copy submitted. Broken or indistinct print, colored or poor quality illustrations and photographs, print bleedthrough, substandard margins, and improper alignment can adversely affect reproduction.

In the unlikely event that the author did not send UMI a complete manuscript and there are missing pages, these will be noted. Also, if unauthorized copyright material had to be removed, a note will indicate the deletion.

Oversize materials (e.g., maps, drawings, charts) are reproduced by sectioning the original, beginning at the upper left-hand corner and continuing from left to right in equal sections with small overlaps. Each original is also photographed in one exposure and is included in reduced form at the back of the book.

Photographs included in the original manuscript have been reproduced xerographically in this copy. Higher quality 6" x 9" black and white photographic prints are available for any photographs or illustrations appearing in this copy for an additional charge. Contact UMI directly to order.

UMI

A Bell & Howell Information Company
300 North Zeeb Road, Ann Arbor MI 48106-1346 USA
313/761-4700 800/521-0600

Automated Tracer-Independent MRI/PET Image Registration

Wei Q. Gu
Department of Electrical Engineering
McGill University, Montréal
Québec, Canada

A THESIS SUBMITTED TO THE FACULTY OF GRADUATE STUDIES AND RESEARCH IN PARTIAL FULFILLMENT OF THE REQUIREMENTS FOR THE DEGREE OF MASTER OF ENGINEERING

November, 1996

ABSTRACT

Existing MRI/PET registration methods are tracer-dependent and may not work well with the PET emission images obtained using tracers which only accumulate significantly in specific regions, or with PET images of pathology which have abnormal tracer distribution.

This thesis describes an automated tracer-independent MRI/PET registration method, in which the registration of MR images to tracer-independent PET transmission images is performed to register the corresponding MRI and PET emission images. Two voxel-based registration methods - mutual information method (**MI**) and voxel intensity ratio (**VR**) method, were implemented for the registration of MRI/PET transmission images.

The validation of the two registration methods was first performed on simulated PET transmission images with real MR images. The quantitative evaluation of these registration results reveals that the **MI** method gives more accurate registration results (mean 3-D registration error less than 2 mm) than the **VR** method (mean 3-D registration error more than 2.5 mm); and the **MI** method is more robust against noise and data truncation than the **VR** method. Both methods are more sensitive to low spatial resolution than to the noise of the PET transmission images. The validation of the **MI** method on real MRI/PET images was also carried out, and the results show no obvious misregistration by visual inspection. Tracer-independent MRI/PET registration using the **MI** algorithm is shown to be a feasible and robust method to register the MRI to PET images, regardless of the tracer used in the PET studies.

RÉSUMÉ

Le recalage de données IRM avec des données PET permet une meilleur interpretation de l'information fonctionnelle fournie par une acquisition PET lorsque ces données sont utilisées conjointement avec des informations morphologiques fournies par des images IRM de haute qualité. Actuellement, les méthodes de recalage IRM/PET sont traceur depéndantes et leur efficacités varient selon que le traceur s'accumule dans des régions anatomiques précises ou que la distribution du traceur est anormale lorsque nous sommes en presence de données PET pathologiques.

Ce travail de thèse décrit une methode de recalage automatique entre données IRM et PET. Cette méthode est traceur indépendante et permet le recalage de données IRM et PET émission par le recalage préalable des données IRM et PET transmission correspondantes. Deux méthodes de recalage basées sur une information de type voxel ont été developpé et implementé durant ce travail de thèse. Ces deux méthodes sont la méthode d'information mutuelle (MI) et la méthode du coéfficient d'intensité en un voxel (VR)

Ces deux méthodes ont été validé dans un premier temps par l'utilisation d'images simulées PET de transmission et de données IRM réelles. L'analyse quantitative des résultats de recalage montre que la methode MI peut donner des résultats de recalage plus precis que la méthode VR. error de recalage est inférieure a 2 mm versus error de recalage superieure a 2.5 mm. De plus, la method MI est moins sensible au bruit et à la troncation de données. Les deux méthodes sont plus sensibles à une faible resolution spatiale qu'au bruit des images de transmission PET.

Dans une deuxième étude, la méthode MI a été validé lorsque des données réelles IRM/PET sont utilisées. Cette étude montre que cette méthode n'entraine pas d'erreurs explicites de recalage, base sur une inspection visuelle des résultats.

En conclusion, le recalage de donnees IRM/PET par une methode traceur-indépendante basée sur l'algorithme MI est une méthode robuste de recalage, quelque soit la nature du traceur utilisé durant l' acquistion PET.

Acknowledgements

I wish to sincerely thank my supervisor, Dr. Alan Evans, for his invaluable guidance, encouragement, and support throughout the course of this project. It has been a rewarding experience working under his supervision.

I would like to thank Dr. Louis Collins, for his stimulating conversation and helpful suggestions. His painstaking work on reviewing my first thesis draft is greatly appreciated.

I would like to extend my recognition to Yilong Ma for his helpful comments and the work he has done in simulated PET study. His work is essential for validation of the methods in this project.

I am also indebted to many members of the Brain Imaging Center at Montreal Neurological Institute for their enlighting discussion. I would specifically like to thank Greg Ward, Vasco Kollokian and Peter Neelin for their implementation of many valuable tools and technical support

I am grateful to Eric Johnstone for proofreading this thesis, and to Dr. Frederic Lachmann for translating the abstract.

I am deeply grateful to my parents for the education they gave me, for their unconditional love, and for their continuous support.

Finally, I would like to thank my wife, Qiao He, for her patience, support and encouragement in the last several years. Her care, love, and deep belief in my capabilities enable me to finally finish this thesis.

Contents

List of Figures

List of Tables

Chapter 1

Introduction

1.1 Background of Image Registration

In the last several decades, many new medical imaging technologies, such as computed tomography (CT), magnetic resonance (MR), positron emission tomography (PET), and single photon emission computed tomography (SPECT) have been introduced into clinical use. These imaging technologies greatly improve clinical diagnosis, treatment planning, and therapy evaluation. Furthermore, since the images from these imaging modalities can provide complementary information, correlating the information contained in different images has been a widely employed approach in both research and clinical environments.

One of the applications to combine complementary information from different imaging modalities is the investigation of functional PET images with the help of anatomic MR or CT images [1, 2, 3, 4, 5]. PET images can produce *in vivo* quantitative measurement of various functional parameters on a regional basis in the human brain, including local hemodynamics, metabolism, receptor kinetics, and tissue pH [6, 7, 8]. However, PET images suffer from poor spatial resolution and a possible low signal-to-noise ratio (SNR). Moreover, poor counting statistics and inadequate reflection of underlying anatomical variation by the distribution of the radiolabel limit the

ability of PET images to yield accurate anatomic information [1]. This may be due to the limited distribution of a tracer, which only accumulates in specific regions, or because the normal distribution is disturbed by the presence of large pathological areas. Hence, it is often hard to identify the location of the functional activity that a PET image indicates. High resolution MR images can provide detailed anatomic information about the human body, but offer no functional information (except for fMR images) as PET images do. Consequently, by combining MRI data with PET data, information concerning physiological activations contained in PET images will be more accurately interpreted with the help of underlying anatomic structures provided by MRI data. Besides the applications in research environment, combining MRI/PET image from the same patient is also useful in the clinical environment. For example, PET images can identify the regions of high metabolic activity or protein synthesis, which are areas of possible cancerous tissue. Accurate localization of the cancer will be greatly enhanced by correlating a PET image with a MR image from the same patient.

Because the images involved in information correlation are acquired at different times, the variations in patient position, and differences in image spatial resolution and voxel size make it difficult for examiners to visually correlate the images accurately. Therefore, explicit registration of the images from different modalities is a necessary step for information integration.

Image registration (sometimes called image fusion, image matching, or image correlation) is the technique to find the geometric transformation which will spatially align the two image data sets in a common space. Although there were many attempts to fuse two images at acquisition time [1, 9, 10], most attention has been paid to 3-D retrospective registration, and it is also the interest of this thesis. In retrospective 3-D registration, one of the two data sets is usually called the target volume, and is taken as the reference volume; the other one is called the source volume, on which a linear geometric transformation (usually containing three rotation and three transla-

tion parameters) is applied to align it with the target volume. Once the geometric transformation has been found, the source volume can then be re-sampled via this geometric transformation. The superimposition of the re-sampled source volume on the target volume enables the voxel-to-voxel comparison of the two data sets either by visual inspection or by using digital operations on the two aligned data sets.

Figure 1.1 illustrates the image registration procedure and a comparison setup of two image volumes. In the first row of the figure, the left image denotes the source image volume, and the middle one is the target volume. The right image shows the superimposition of the source and the target image volumes. It should be noted that the superimposition is done in a common coordinate space. It can be seen from the figure that due to different orientations of the head during two separate scanning sessions, the two volumes are not aligned in the same coordinate space. Image registration procedure is applied to the two images to find a geometric transformation to align them. After the registration procedure, the source volume can be re-sampled by the registration result and the transformed source volume (left image in bottom row) can then be superimposed on the target volume, allowing direct voxel-to-voxel comparison.

1.2 Key Elements in Image Registration

The framework for the image registration method can be viewed as a combination of four key elements as follows [11]:

- Extracting Matching features. The matching features consist of information extracted from the original images which is used for matching. This may be explicitly-defined corresponding features such as anatomical landmarks or surfaces identified in each image. Alternatively, there may be no specific corresponding features defined but registration is achieved by alignment of some intensity-derived property of the images.

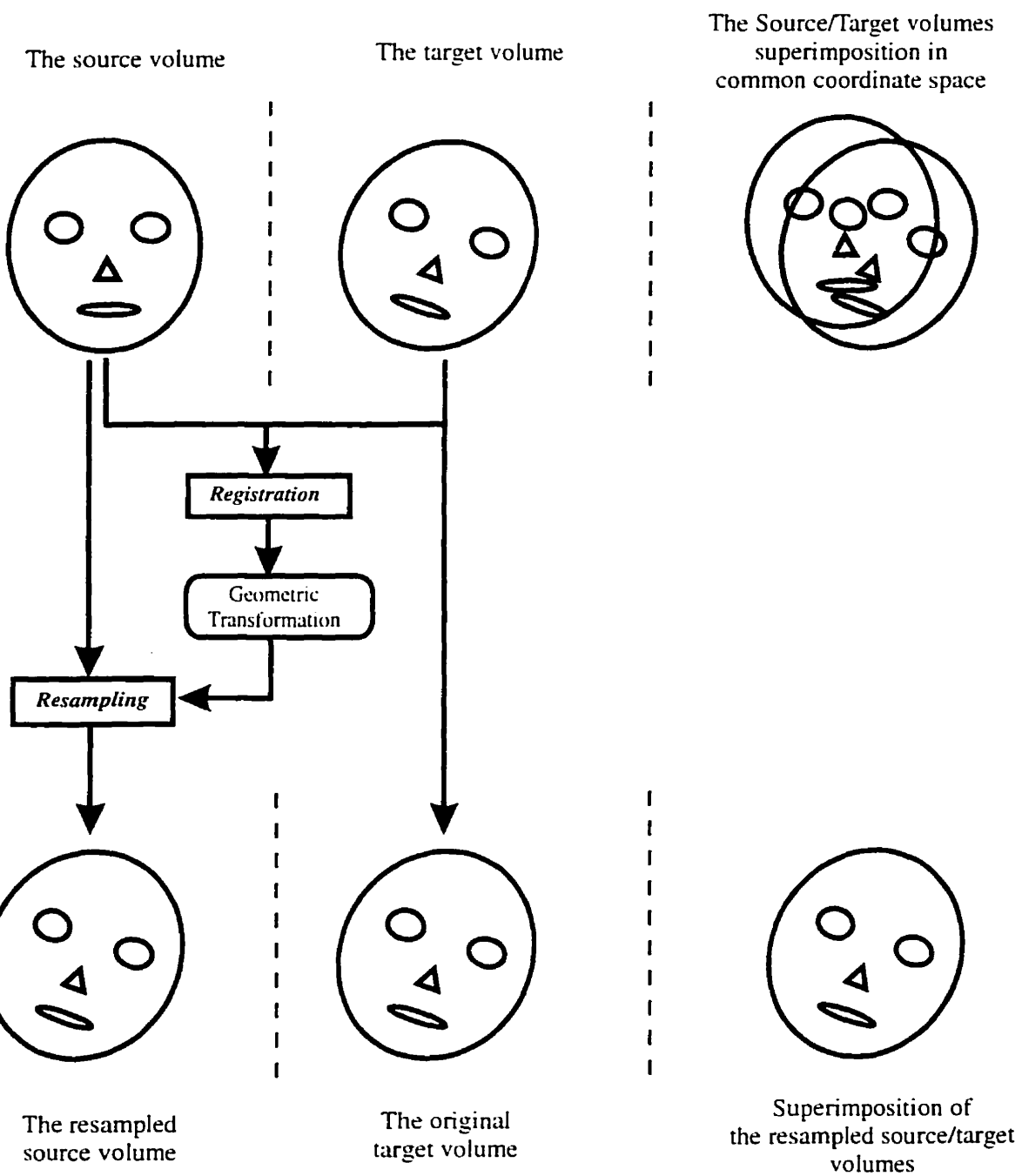

Figure 1.1: Image registration procedure.

- Parameter search space. The searching space is a set of transformations which is used to resample the source image to align it with the target image. The extension of the searching space is determined by the problem itself. For example, in 2D image registration, there are usually three parameters in the geometric transformation - two translations and one rotation; while in 3D image registration of rigid bodies (as in intra-subject registration), there can be six parameters - three translations and three rotations. The complexity of the searching procedure is partly determined by the number of these transformation parameters.

- Similarity measurement. The similarity measurement is the criterion used to measure how well the source image aligns with the target volume after the source image has been re-sampled by the current transformations in the parameter search space. For example, the sum of absolute differences between corresponding voxel values from two images may be taken as a similarity measurement. When the sum is minimized, the two images are assumed to be optimally registered.

- Optimization procedure. Since the registration is a procedure to find the best transformation which leads to an optimal similarity measurement on the matching features, an optimization method is a necessary component in this problem domain.

The choice for each element is important for a successful final result of the image registration and has great impact on the other elements. For example, a matching feature which can be easily detected by image processing techniques might eliminate the necessity of human intervention in the registration procedure. A good similarity measurement defined on the matching features may cause fewer local extremes in the parameter search space, which will greatly relieve the burden from the optimization procedure and make the registration method more robust.

1.3 Monomodality and Multimodality Image Registration

Depending upon the sources of the images engaged in the registration problem, there exist two kinds of image registration - monomodality and multimodality registration.

Monomodality image registration tackles the registration problem for two or more images from the same image modality. This category can be further divided to intra-subject and inter-subject registration.

Intra-subject monomodality registration focuses on the same patient's images which are acquired at different times [12, 13, 14, 15]. As an example, accurately aligning two X-Ray images from the same patient acquired at different times might be useful to detect, locate, and measure pathological changes in a target organ. Inter-subject single modality image registration is useful in assessing morphometric variability over large number of patients [16, 17, 18]. Although both source and target images are from the same modality, inter-subject registration is an interesting problem, due to dissimilarity in sizes and shapes of subjects' brains and is the subject of much recent research.

Multimodality image registration is the registration of two image volumes from different modalities, usually from the same patient. Combining anatomical and functional images [4, 5, 19] from the same subject can lead to better interpretation of the functional information. Correlating two anatomic images is also a valuable tool in radiotherapy and radiosurgery. Precise dose localization in radiotherapy requires both precise target contours, which are best outlined from MRI; and accurate dose distribution calculations, which are better derived from the tissue-density information provided by CT [20, 21, 22].

In the intra-subject multimodality registration problem, the difficulty resides in the enormous dissimilarity between the source and the target images. Similar tissue types in the two images may take on very different intensity values, and the problem is

even worse when one of the images records anatomic information and the other records functional information, where the latter might not provide much useful information on anatomic structure.

1.4 Objective of This Thesis

Although existing imaging technologies can be applied to different parts of human body, such as spinal cord, brain and chest; the MRI and PET images from the human brain are the major sources for investigation of brain function at the Brain Imaging Center (BIC) of Montreal Neurological Institute (MNI). Hence, the focus of this thesis is the MRI/PET registration problem as applied to 3-D images of the human brain.

1.4.1 Problems with Existing Methods of MRI/PET Registration

Many methods have been reported for successfully registering MRI to PET emission images [31, 23]. Some of them are manual or semi-automatic needing some human intervention during the registration procedure. Automated MRI/PET registration methods make use of image processing technologies to extract corresponding features from two data sets and search for the best transformation to map these features in a completely automatic way. Both types of methods have advantages; however, this thesis covers the registration of MR to PET images in an automated fashion.

In different PET studies, various tracers are used to measure physiology. For example, [^{18}F]fluorodeoxyglucose (FDG) is widely used in neurology, cardiology and oncology to study glucose metabolism. Many PET tracers measure receptor or neurotransmitter kinetics, for example, [^{18}F]fluoroDOPA can be used to measure the activity of the dopa decarboxylase, a pre-synaptic enzyme involved in the synthesis of the neurotransmitter dopamine.

The existing automatic MRI/PET registration methods only work well with MRI

to some PET images acquired using tracers such as FDG and $H_2^{15}O$ which suffuse the entire brain parenchyma, but not to those obtained by enzyme tracers such as receptor ligands which often provide limited anatomical detail in the emission images. In other words, existing methods are tracer-dependent. Furthermore, for tracers which do accumulate throughout the brain in cerebral blood flow or metabolism studies, registration techniques based on assumptions of uniform tracer distribution can often fail with PET images containing large regions of abnormal accumulations such as in stroke or tumor studies. Figure 1.2 shows a PET emission image acquired using [^{18}F]fluoroDOPA, which does not contain adequate anatomic information for registration purposes.

1.4.2 Tracer-Independent MRI/PET Registration

A PET transmission (tPET) image, usually acquired immediately before the PET emission (ePET) study, is similar to an X-ray CT scan of tissue density but acquired with 511 keV gamma rays instead of the usual 80-100 keV X-rays. It carries the information necessary to correct for gamma-ray attenuation in the tissue which occurs during the subsequent ePET study. Although the tPET image lacks the fine detail of X-ray CT imaging, it can still identify some anatomic structures, such as petrous bones, sinus cavities and skull. This anatomic information is sufficient to register the tPET image with MRI data. Because the tPET and ePET images are acquired in sequence while the patient is immobilized in the PET scanner by a customized foam head-holder, we assume that the tPET and ePET images are spatially aligned. Furthermore, the post-injection tPET scan technique [24] and the simultaneous transmission and emission scan technique [25, 26] in PET greatly reduce or even eliminate the time span between transmission and emission scans, thereby the likelihood of patient motion during scans. This further ensures exact spatial alignment between tPET and ePET data. In a clinical environment, to prevent from possible misregistration between tPET and ePET due to the patient movement in a long time PET

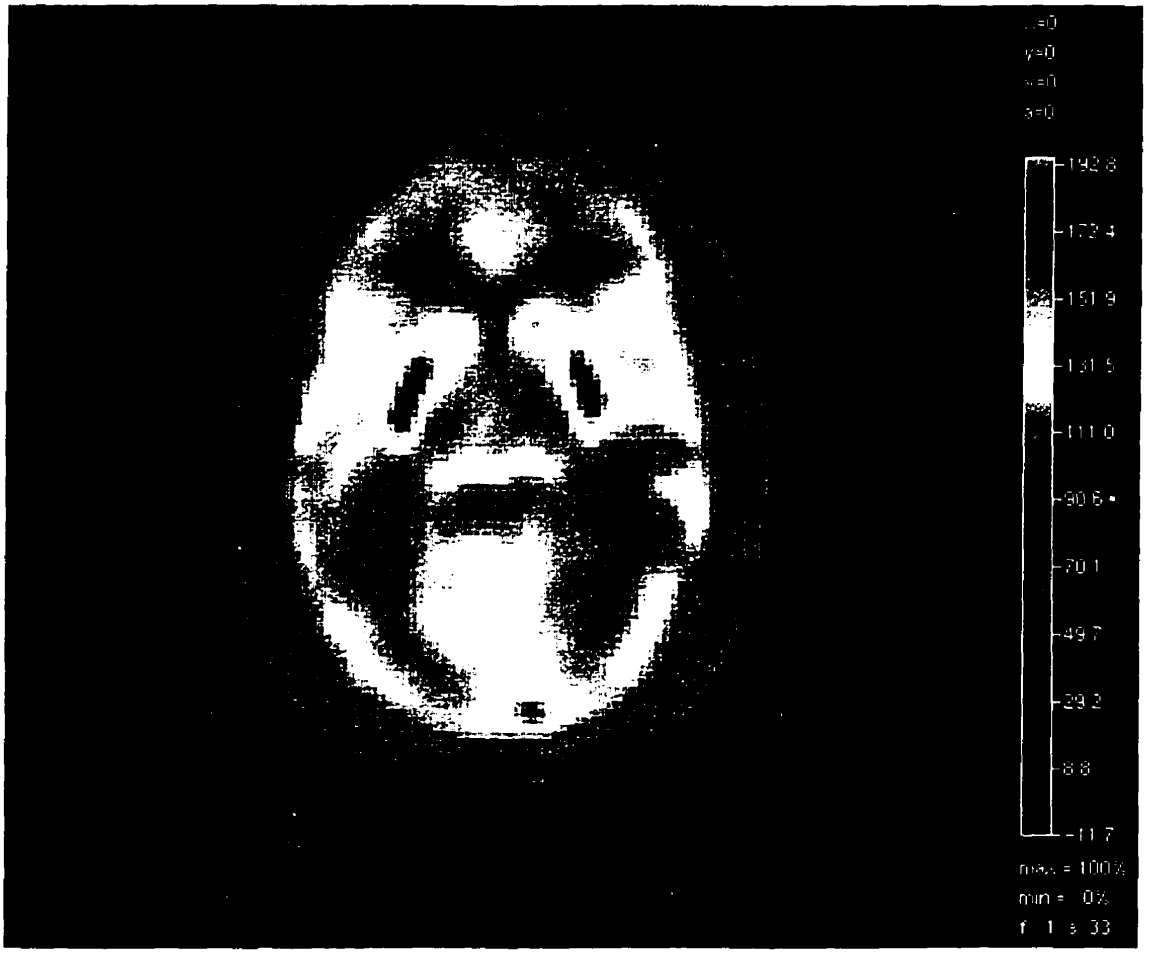

Figure 1.2: A transverse slice of a typical [^{18}F]fluoroDOPA PET image acquired from Siemens ECAT HR+ scanner (FWHM = 8 mm, voxel size = $2 \times 2 \times 2.4$ mm^3 with 63 slices. The slice shows the dopamine distribution in the normal corpus striatum).

scan, several transmission scans can be made along the ePET scan. In this way, a tPET scan will be used for registration of ePET scans made around the time when the specific tPET scan was made, which can also ensure the registration of tPET and ePET images of the same patient.

From the registration of MRI/tPET images, the MRI and ePET image can be indirectly registered. Since tPET images carry the same information regardless of the kind of PET tracer study, MRI/tPET registration allows the registration of MRI to ePET image in a tracer-independent way. Several research groups have tried to use tPET to register MRI to ePET images [4, 77]; however, their methods are either manual or semi-automatic, in which human intervention is necessary to identify matching features. In this thesis an automated registration method which matches MR/ePET image through MR/tPET image registration is investigated.

In summary, the objective of this thesis is to find an accurate and robust method which will register MRI to tPET images; and thereby accomplishing MRI/ePET image registration automatically.

Due to the limitations of tPET images and characteristics of multimodality image registration, it is also desirable that the MRI/tPET registration be stable when:

- the tPET image is at low spatial resolution;
- the tPET image has low signal-to-noise ratio (SNR);
- the MRI and tPET data do not cover exactly the same volume of brain.

1.5 Structure of This Thesis

In this thesis, chapter 2 briefly describes the basic principles of positron emission tomography and the relationship between tPET and ePET images. Chapter 3 gives a review of existing multimodality image registration methods. In chapter 4, the methods for MRI/tPET image registration used in this thesis and some implementation

details of the algorithms are described. Validation methods on the registration algorithms are also presented in this chapter. Chapter 5 presents the experiments and results of MRI/simulated-tPET image and MRI/real-tPET image registration. Several implementation details are explored first in this chapter; and then experiments are carried out on simulated tPET images generated by setting scanning parameters close to those used in clinical studies; finally the robustness of the method to various resolutions, SNR, and data truncation is explored. Discussion of the experimental results and a comparison of two registration methods are also given in this chapter. The last chapter draws conclusions from the experimental results; and possible future work is proposed to end this thesis.

Chapter 2

Positron Emission Tomography

Positron emission tomography is a technique used to study the distribution of substances labeled by positron emitting radioisotopes within a three-dimensional object. The radioisotopes are first injected or inhaled into the body, and by making use of measurements of radiation from these isotopes, an intensity image can be reconstructed from the recorded radiation data. The intensity of voxels can be regarded as the representation of the isotope concentration.

Many comprehensive papers are available giving detailed information about the positron emission tomography technique [27, 28]. In this chapter, only the basic principles of PET and the characteristics of PET images are briefly described.

2.1 Positron Emission and Detection of Emission

Positrons are positively charged electrons. The nucleus of some radioisotopes, which have an excessive number of protons, can emit the positrons to stablize the nucleus by removing the positive charge. Although proton-rich radioisotopes can reduce excessive positive charge in the nucleus by another way in which the nucleus captures an orbital electron and neutralizes the positive charge, all radioisotopes used in the PET technique decay by positron emission.

After traveling a short distance (the distance depends on the energy of the positron, i.e. for F-18 the maximum range of the distance $\approx$ 2.6 mm) , a positron emitted from a decaying nucleus will collide with a surrounding electron. The annihilation caused by the collision will convert the masses of both positron and electron into electromagnetic radiation. In order to conserve the energy and linear momentum, the electromagnetic radiation takes the form of two 511 keV gamma-ray photons at $180° \pm \frac{1}{4}°$ apart from each other. The two photons are often called *coincident rays*. Easily penetrating the human body, the coincident gamma-ray photons are then recorded by external detectors. Because the two annihilation photons are emitted at 180° to each other and they are created at the same time, the near-simultaneous detection of the two photons by a pair of detectors placed opposite to each other can determine the localization of the emission to be limited to the line joining the two detectors. If only one of the photons is detected, the annihilation must have originated from the region outside the volume between the detector pair or the other ray was lost by scattering or absorption in the scanned object. In this case, the detected event will be rejected.

Figure 2.1 is a schematic diagram of coincident ray detection. Two detectors are placed on the opposite sides of the object. The region (often called *sensitive volume*) encased by the detector and the two dashed lines is an area in which true coincidence event can be detected. In the diagram, it can be seen that another coincident event that happened outside of the sensitive volume is rejected by the detectors since only one gamma-ray photon is detected.

The detection of the annihilation coincidence is in one dimension only. To obtain a three dimensional image, it is necessary to get the measurements from different directions. This procedure is in essence similar to other tomography techniques, such as computed tomography (CT). Once enough measurements have been obtained, the data can be reconstructed into a two-dimensional tomographic image [29, 30].

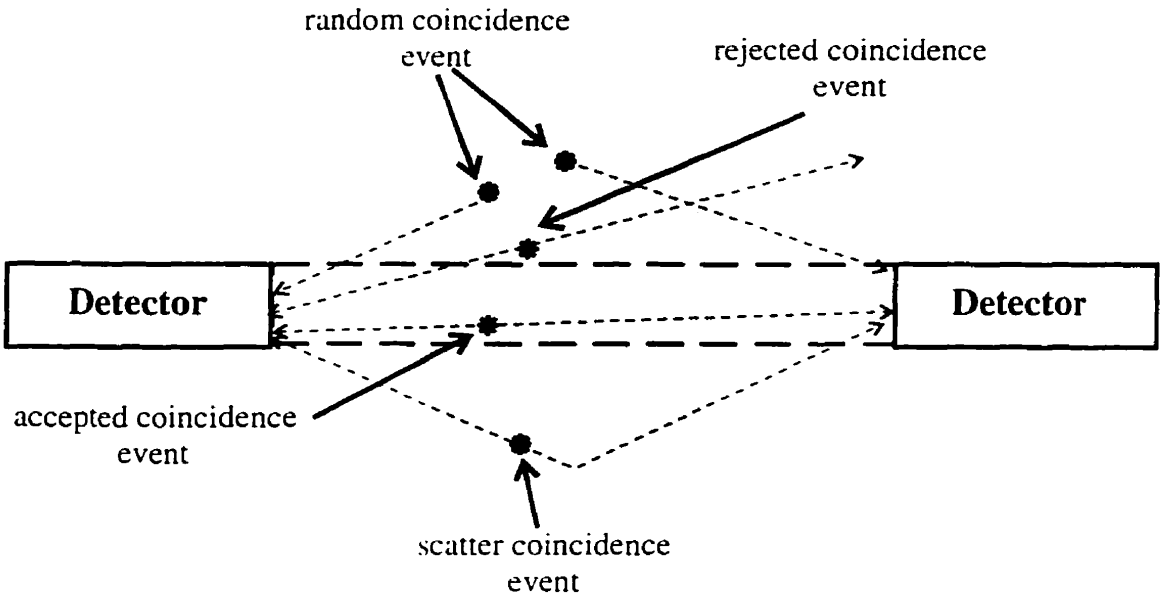

Figure 2.1: Detection of positron emission.

2.2 PET Transmission Image

As the annihilation photon penetrates human body, it may lose some of its energy or even be absorbed. This attenuation of photons is one of the major sources of inaccuracy of PET image. The emissions that occurred in the center of the human body will be attenuated more than the ones near the surface of the body due to the longer distance between the emission and the detector. Without attenuation correction, the measurement of annihilation photons can not truly represent the concentrations of isotopes in the body. The attenuation of radiation after photons pass through an object can be represented as:

$$I = I_0 e^{-\mu x} \tag{2.1}$$

where I_0 and I are the original number of photons and the number of photons left after passing through the object respectively; x is the distance of the radiation traveling within the attenuation object; and μ is the attenuation coefficient of the object.

One way to measure the attenuation correction is to generate a PET transmission image. In order to get the attenuation factor for the subject, two additional scans are

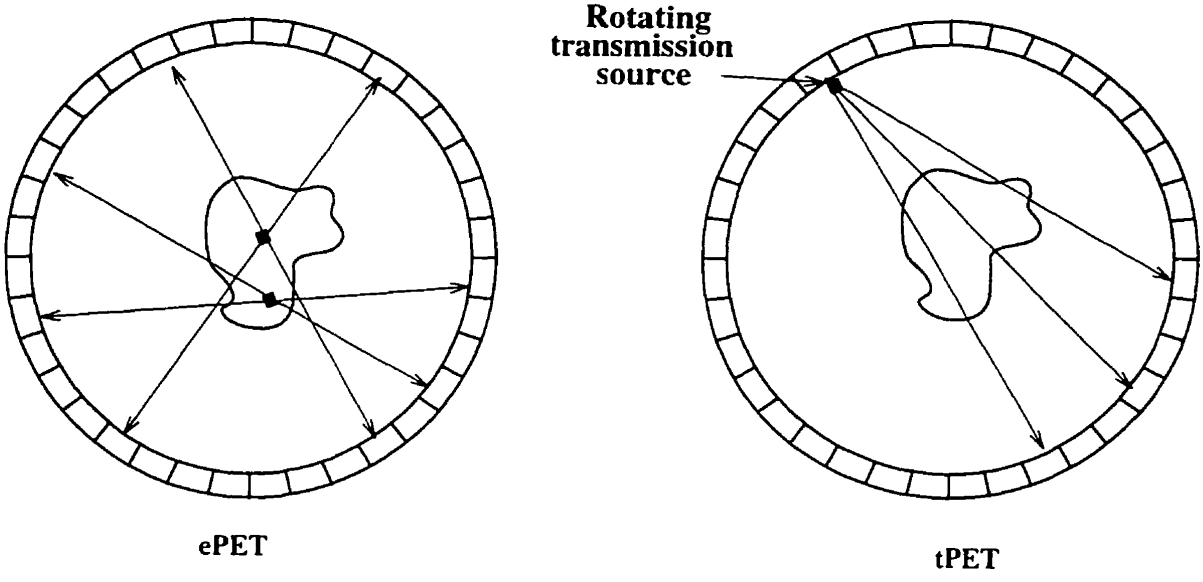

Figure 2.2: The Geometry of ePET and tPET Scans

needed before the emission scan. With a ring positron emitter placed in the field of view (FOV) of the scanner, the scanner first does a blank scan of the emitter source without the subject in the FOV before it scans the subject of interest (transmission scan).

For every line-of-response between two PET detectors i and j, LOR_{ij}, the blank scan data and transmission scan data measure I_0 and I respectively in Equation 2.1. The ratio of the two data sets can then be used to compute the attenuation correction for the corresponding LOR_{ij} from the ePET scan. The log of this ratio (μ in Equation 2.1) can be reconstructed to provide an image of the attenuation coefficients of the cross section in a fashion analogous to the reconstruction of the ePET image. This image is called the PET transmission image (tPET). Figure 2.2 shows the geometry of ePET and tPET scanning.

In principle, the formation of a tPET image is the same as that of an X-ray CT image. Although the actual image quality of the tPET image is much worse than CT image, it can still delineate some of the important anatomical structures such as

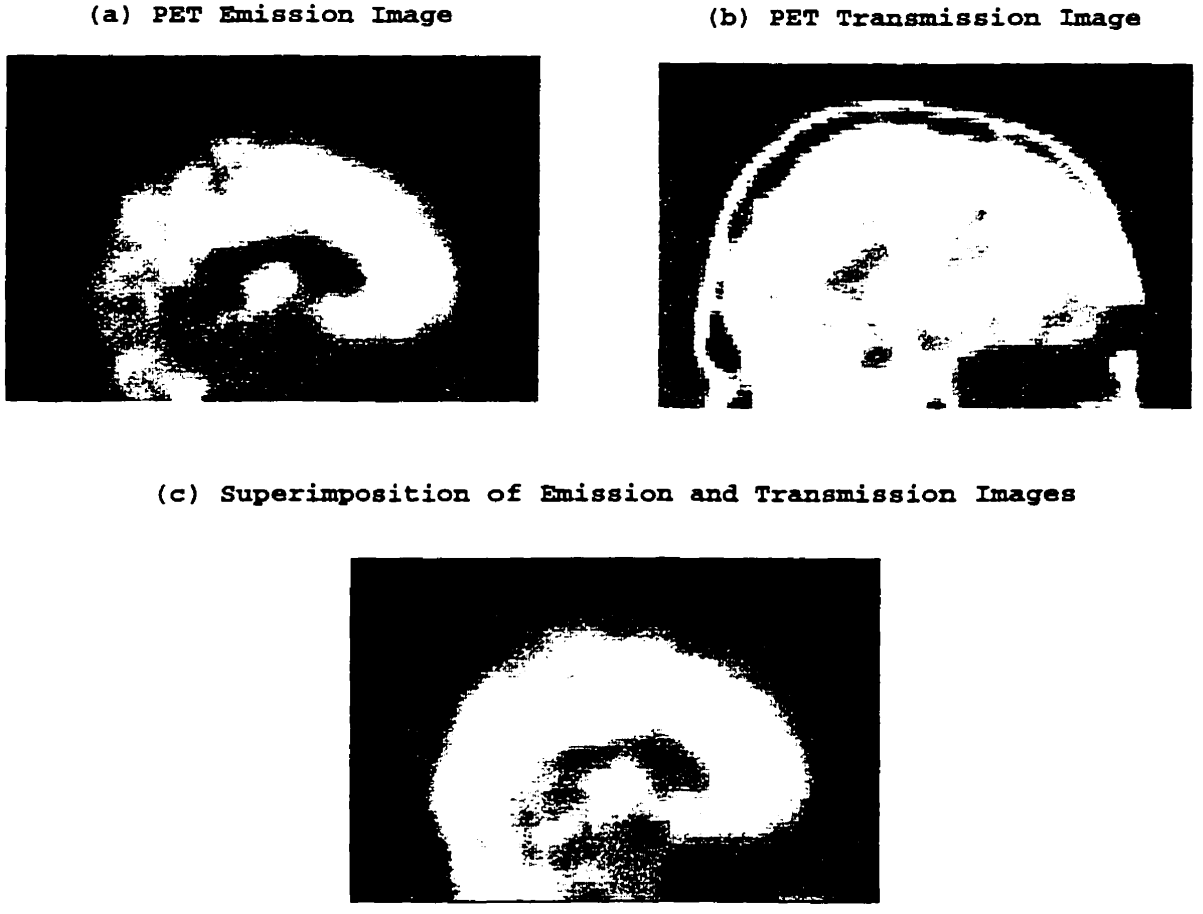

Figure 2.3: PET emission and transmission images

bone. Figure 2.3 shows sagittal slices from a ePET image and from a corresponding tPET image. These PET images are obtained from a Siemens ECAT HR+ scanner (FWHM = 8 mm, voxel size = $2 \times 2 \times 2.4$ mm^3 with 63 slices) in a $H_2^{15}O$ tracer study.

2.3 Characteristics of the PET Image

2.3.1 Spatial Resolution of the PET Image

Ideally, the spatial resolution of a PET image is determined by the detector width of the PET scanner. In reality, there are two more factors which will reduce the accuracy of positron emission localization detected by the scanner, and thereby lowering the spatial resolution of the final image [28]:

- Not all annihilation photons are emitted at exactly 180° (i.e. $180° \pm \frac{1}{4}°$) due to the residual momentum of the emitted positron;
- The positron travels some distance (i.e. for F-18 the maximum range of the distance $\approx$ 2.6 mm) from the site of the emitting nucleus before annihilating with an electron. This distance depends on the energy of the positron.

Moreover, if there is patient motion during scan, it apparently will cause resolution loss (i.e. blurring) in the final image. There are three aspects of effort to remedy this problem:

- a comfortable scanning setting to allow the patient to be at ease during scanning;
- a short scan time;
- a well-designed restraint system.

2.3.2 Noise

In the section 2.1, an ideal detection of positron emission was described. However, in reality, there are two kinds of spurious events which can be mistakenly accepted as coincidence rays (shown in Figure 2.1) – scatter coincidence and random coincidence.

Because of the interaction with surrounding tissues, the annihilation photons can scatter from their original direction. In Figure 2.1, a coincident event that happened

outside the sensitive volume is detected simultaneously by the two detectors due to scatter.

The random coincident event accepted by the detectors is actually two photons from different emissions which happen to reach the two detectors at almost the same time. Due to the speed limitations of the detector itself and the finite speed of gamma rays, the detectors cannot distinguish the random event from the true coincident event.

Both scatter and random events will cause artifacts in the final PET image. Together with other noise sources (i.e. detection efficiency) which will not be discussed in detail here, the artifacts contained in the data set make PET images have lower signal to noise ratio (SNR) than the MR images.

2.4 Summary

From the above sections, it can be seen that due to the physics of the emission process and the physical size of the detectors, both ePET and tPET images have very poor spatial resolution. With such a low spatial resolution, the partial volume effect [1] is also a problem associated with PET images. When compared with MRI and CT images, PET images usually have lower SNR due to low counting rates, scatter coincidences, and accidental coincidences.

Despite the above limitations, PET image can provide *in vivo* measurement of a wide variety of functional parameters in human brain. These functional measurements can greatly improve the understanding of human brain function and provide an effective way to detect the abnormal function of tissues.

[1] Refers to the case of a data element (pixel or voxel) containing more than one tissue type.

Chapter 3

Review of Multimodality Image Registration Techniques

In this chapter, a review of multimodality image registration techniques is presented. The goal is not to cover all of the existing image registration methods, but to focus on the methods for three dimensional multimodality medical image registration problem.

Many methods have been proposed to deal with the medical image registration problem (see [23, 31, 32] for an extensive literature review). Since the focus of this thesis is the intra-subject registration of MRI/PET images, this review is limited to 3-D linear registration methods, where a global [1] linear [2] transformation is used to re-sample the source volume to align it with the target volume.

In Chapter 1, the four key elements in the framework of an image registration method were described. Four categories of methods will be discussed in this chapter as follows:

- Point-landmark-based methods,

[1] A transformation is called global when a change in any one of the matching parameters influences the transformation of the image as a whole. [31]

[2] In this thesis, we define the linear transformation as a transformation only including translation, rotation and isotropic scale.

- Surface-based methods.
- Principle axis transformation method.
- Voxel-based methods.

Although the optimization methods will not be covered in this review, it should be noted that this element is important to the accuracy and robustness of the registration methods. Two registration methods using the same matching features but different optimization methods may yield very different results. Also, a better optimization method may allow a more accurate registration result with faster convergence speed.

3.1 Point-landmark-based Multimodality Registration Methods

Point-landmark-based methods use small sets of homologous point landmark pairs from both the source and the target images as the matching features. The points to be matched are obtained from either external fiducial markers or intrinsic anatomical landmarks in the images themselves.

3.1.1 Extrinsic Landmarks

The points to be matched can be obtained from external fiducial markers. These markers are attached either to the head of the patient directly [33, 34, 35, 36] or to a structured fiducial frame fixed to the patient's head [37, 38, 39, 40, 41, 42, 43]. Ideally, the fiducial makers should meet the following requirements to generate the appropriate landmarks for the registration:

1. The markers should appear in both modalities (i.e. MRI and PET); and the image of the markers in both modalities should have high contrast when compared with surrounding structures for ease of identification.

2. The locations of the markers can be accurately identified. The accuracy of their localization should not be worse than the spatial resolution of the images from each modality.

3. The markers should be comfortable for the patient to wear and easily attached to or detached from the patient.

4. The markers should not cause artifacts (e.g., magnetic susceptibility or chemical shift in MRI) in both image modalities. Otherwise they will deteriorate the quality of the image, and furthermore, affect the following processing and analysis.

The fiducial markers might not satisfy all of these requirements in practice. For example, the locations of the markers in a stereotactic frame fiducial marker system can be identified accurately from both images, but it is uncomfortable for the patient to wear and might cause artifacts in the MR images. On the other hand, markers attached to the skin of the head lets the patient feel more comfortable during the scanning. However, there is a possibility of skin movement between or during image acquisitions, and the fiducial markers might not be fixed steadily relative to the subject. Therefore, this kind of marker system is mostly used in the case where one of the image modalities produces a lower resolution image than the other one does, such as in MRI/PET registration.

3.1.2 Intrinsic Landmarks

Another way to obtain corresponding landmark pairs is to identify the equivalent points in the two images based on anatomical structures [5, 44, 45, 46]. A user, who has enough radiological knowledge of the anatomy of structures in both modalities, can use a display and navigate software to search for corresponding tag (either intrinsic or extrinsic) points on both the source and the target images. After the corresponding points are identified from the two images respectively, the co-registration

transformation can be obtained by minimizing some distance norm between these point landmarks.

A widely used distance norm in point-landmark-based registration methods is the least square fit [49] [51]:

$$lsq^2 = \sum_{i=1}^{N} \| Q_i - T * P_i \|^2 \tag{3.1}$$

where P_i and Q_i $(i = 1....N)$ are the the set of landmark pairs for the source and the target volumes respectively, and the 3-D transformation applied to the source volume is represented by T. $\| \cdot \|$ is the notation for norm of vector. When the geometric transformation minimizes the lsq^2 term, the transformation is taken as the solution for the registration of the two data sets.

Unlike the other registration methods discussed below, the optimization procedures in landmark-based registration methods are not iterative. The direct solution from linear algebra makes the optimization very efficient. The Procrustes algorithm [47, 48] was used by Evans et al. [5] to minimize the least square measurement.

Since the locations of landmark points are determined by the user, the accuracy of the points' location depends on the expertise of the user, the type of data (i.e. MRI, PET) and image quality (i.e. contrast and spatial resolution). Therefore, a friendly user-interface for the labelling operation is a key component for the success of this method.

Moreover, two factors affects the accuracy of the intrinsic landmark registration approach:

- homology error, i.e. uncertainty in identifying the equivalent landmarks from the two images;
- the number of landmark points used in the registration.

Neelin et. al. used point simulations to investigate the effect of these two factors on the intrinsic landmark registration method [77]. Figure 3.1 (from [77]) shows their result. A constant homology error $\sigma_h = 5mm$ was injected into the simulation. The

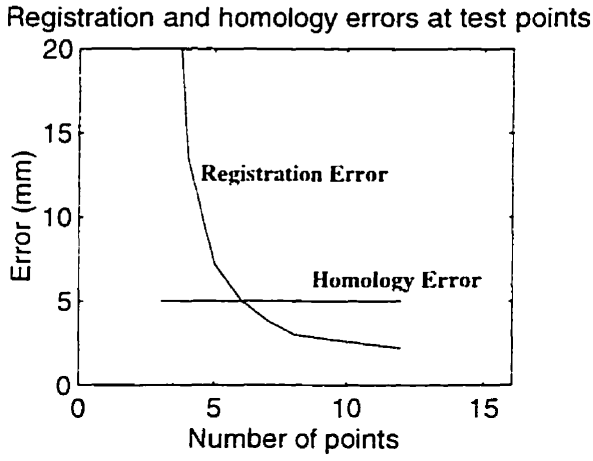

Figure 3.1: Registration and Homology Error in Intrinsic Landmark Registration Method.

registration errors fall rapidly with N (the number of points used in the registration) when $N < 5$. But when N is between 8 and 10, the registration error is proportional to $\sigma_h/\sqrt{N}$. Similar curves were observed from their experiment, for injected noise levels of 2, 10, and 15, with the error scaling linearly with noise level.

3.1.3 Discussion

Once the point landmark pairs are identified, the point-landmark-based registration methods have the advantage of computational efficiency. The direct solution of the optimization increases the robustness of this method over the iterative approaches.

However, the extrinsic landmark method complicates the image acquisition process and makes retrospective analysis impossible. Placing the external fiducial markers on patient's head is inconvenient for the patient and may be expensive as well. Furthermore, if the markers are attached to the skin, landmark location may not be accurate since skin movement will be inevitable. The intrinsic landmark method relieves the patient from any external attachments; and it enables the retrospective registration since no prescan procedure is required. But the accuracy and robustness of this method depends heavily on the expertise of the user. This method is also time

consuming due to difficulty in identification of low contrast anatomic structures, especially in anatomical/functional image registration, such as MRI/PET or MRI/SPECT registration. With respect to human interaction during the registration procedure, extracting the coordinates of external fiducials is usually straightforward and can be automated; the intrinsic point-landmark-based registration methods require manual interaction to identify the landmark points.

3.2 Surface-based Multimodality Registration Method

In order to overcome the difficulty of identifying anatomic structures in low contrast medical images, many researchers have proposed to use corresponding surfaces from the images as matching features to fulfill the registration [4, 52, 53, 54]. In most medical image modalities, continuous surfaces are more easily labelled than specific point landmarks. For example, the contrast between air and tissue is high in MRI and CT, which makes it easy to extract as boundary or surface feature from original images.

One of the popular surface-based registration methods is referred to as the *head and hat* algorithm [4]. The surface obtained from the first image, which is usually at higher resolution, is represented by a set of 2-D contours extracted from the slices of the tomographic image. For instance, the external surface of tissues in MRI or CT images is easily outlined; these contours form the *head* model. The corresponding surface from the second image is usually represented by series independent points, and is referred to the *hat*. After the *head* and *hat* are acquired, the *hat* surface is transformed to fit the *head* surface. The registration result is finally obtained when the *hat* surface most closely fits onto the *head* surface. Usually, the measure of fit between two surfaces is defined as the square of the distance between a point from the *hat* and the nearest point on the *head* surface in the direction of the *head*'s centroid. However, this measure of fit has a problem that the point on the *head* surface, which

is nearest to a point on the *hat*, might not be in the direction of the *head*'s centroid. The author claimed the mean registration error of MRI/PET registration is below 2.5 mm. Several research groups improved the fit measurement by applying distance transforms to images, which can be performed efficiently by the chamfer method [55, 56, 57].

In some cases, it is difficult to identify the equivalent high contrast surfaces from the two images to be registered. For example, the inner surface of the skull is distinct in CT images while it is not very clear in MR images. Hill and Hawkes [58] proposed using adjacent anatomical structures instead of exactly equivalent structures as matching features. In their method to register MR and CT images, the inner surface of the skull from the CT image and the outer surface of the brain from the MR image are first extracted from the original images. Although the two surfaces are not exactly equivalent to each other due to the presence of membranes, blood vessels, etc., between them, knowledge about the relationship between the two surfaces (i.e. containment relation) can still help to define a fit measurement between the two surfaces, which can lead to an optimal geometric transformation to align the two image volumes.

Surface-based methods take a further step towards automating the medical image registration procedure. Since numerous edge and boundary detection methods already exist, the extraction of a surface from the 3-D volume can be automated, hence relieving the burden of detecting equivalent anatomic structure from users. However, the existing edge and boundary detection methods are far from accurate and robust on real medical images. Therefore, some user interaction is usually still needed to accurately extract the surfaces from the images.

3.3 Principle Axis Transformation

The principle axis transformation (PAT) method introduced by Alpert et al. [19] is an analytic approach based on the classical theory of rigid bodies [50]. A rigid body can be uniquely localized by the position of its center of mass and the principle axes [3] with origin placed at the center of mass. Rigid bodies can be constructed by extracting an equivalent surface from each image and taking the surface-enclosed volume as a 3-D object of uniform density. Once the rigid bodies have been defined from the images, the center of mass and principle axes can be obtained for each object. In the PAT method, one rigid body is first translated to make the two bodies' centers of masses coincident, then the necessary rotational operations are applied to align the two rigid bodies, thereby registering the two images. This approach, as the author claimed [19], can accomplish with typical errors in the range of around 1mm.

The principle axis transformation has the advantage of an analytic solution. It avoids the heavy computation and local-minima problem associated with the iterative registration techniques. However, this method is sensitive to truncation of one or both of the image volumes [23], which yields nonequivalent objects and different moments of inertia for the two images.

3.4 Voxel-based Multimodality Registration Methods

The point-landmark-based, the surface-based, and the PAT registration methods achieve their goals by matching correspondent features extracted from the original images. Due to the fact that accurately identifying corresponding features is not easy and is sensitive to noise and data truncation, these methods require some user intervention during the registration procedure. Furthermore, in some cases, if the contrast

[3] Orthogonal axes about which the moments of inertia are minimized.

is low between the feature of interest and surrounding tissue, it is even difficult for an operator to visually detect the corresponding features from both images. Voxel-based registration methods, which are based on the numerical comparison of all or a large number of voxels from the two images, usually do not require an accurate feature extraction step.

The assumption in voxel-based methods is that a numerical operation between each corresponding voxel pair will provide a similarity measure, which is optimal when the two images are correctly registered. Therefore the similarity measurement is the most important element in the voxel-based methods; in contrast, the accuracy in identifying corresponding features largely determines the success of the point-landmark-based and surface-based registration methods.

Three similarity measurements proposed for multimodality medical image registration will be discussed in the following sections: cross-correlation, variance of voxel intensity ratio, and mutual information.

3.4.1 Feature Space Histogram

The feature space histogram, sometimes called a scatter plot, is a very useful tool for examining the effects of misregistration. Since most voxel-based methods reviewed in this chapter are directly or indirectly related to the analysis of the feature space histogram, a brief description of the histogram and its characteristics is given here first.

The feature space histogram is in principle a 2D histogram ($h(x, y)$) of spatially aligned voxel intensity pairs from the source and the target volumes respectively. The variables of x and y are the intensity values of voxels from the source and the target image volumes having the same spatial coordinates. The value of $h(x, y)$ is the number of the voxel pairs, such that the intensity value of the voxel from the source volume is x, and the intensity value of the aligned voxel from the target volume equals to y. Equation 3.2 illustrates the structure of the feature space histogram:

$$h(x,y) = Number(P_s, P_t) | P_s = P_t, I(P_s) = x, I(P_t) = y) \quad (3.2)$$

where P_s, P_t are the coordinates of the voxels from source and target volumes respectively, and $I(P)$ represents the intensity of the voxel at P.

The shape of the feature histogram has a close relationship to the image misregistration. To explain this relationship, a feature space histogram sequence of registered and misregistered images was generated (shown in Figure 3.2). For simplicity, a T1 MR image was chosen for both source and target volumes. In the original setting, the source and target volumes were strictly aligned because they are identical. Since the two images are exactly the same, the feature space histogram (Figure 3.2 (a)) is a straight diagonal line when the two images are registered. In Figure 3.2 (b), (c) and (d), the source image is shifted by 3 mm, 5 mm, and 10 mm from its original position along the x direction respectively; in (e), (f), and (g), the source image is rotated around the x direction for 3°, 5°, and 10° respectively.

It is very clear that as the two images are misregistered, dispersion from the diagonal line in the feature space histogram is increased.

A feature space histogram sequence from MRI/tPET data was also generated (shown in Figure 3.3). This time the two images were acquired from different modalities and there is no monotonic relationship between MRI intensity and tPET intensity. The relationship between the scatter plots and misregistration is not so clear as it was shown in Figure 3.2, but the dispersion of the scatter plot with misregistration can still be observered. The "cloud" in the feature space histogram becomes less tight as the two images are moved farther from the registered position.

3.4.2 Cross-Correlation Method

Cross-correlation has been widely used in signal processing to measure how closely two signals match each other. Thus, it is very natural to use cross-correlation in image registration. In three dimensions, for volumes A and B with $I \times J \times K$ dimensions,

(a) registered

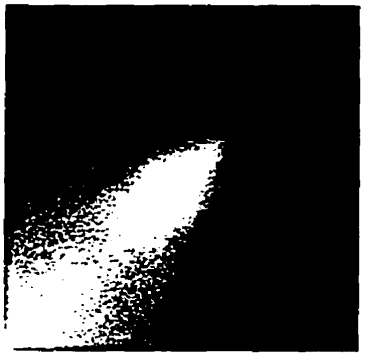

(b) shifted 3 mm

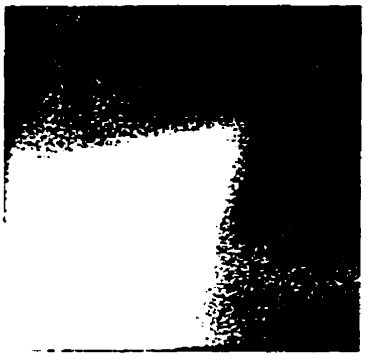

(c) shifted 5 mm

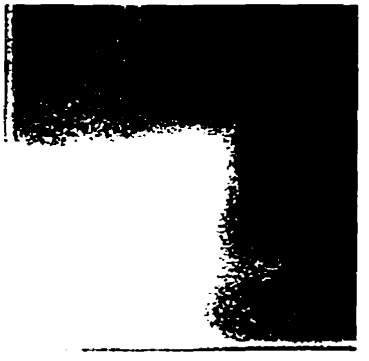

(d) shifted 10 mm

(e) rotated 3°

(f) rotated 5°

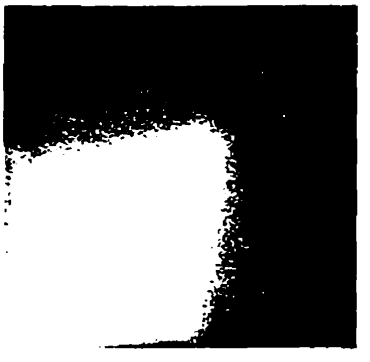

(g) rotated 10°

Figure 3.2: Feature space histogram and image misregistration

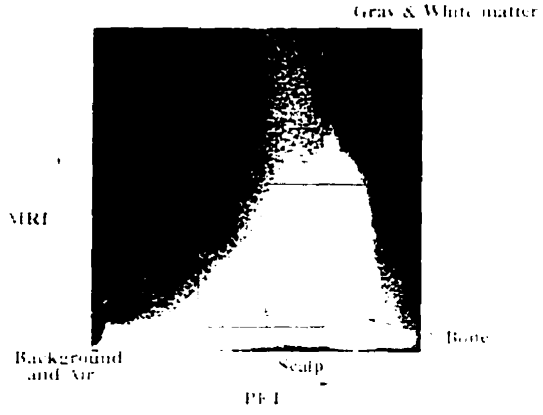

(a) registered

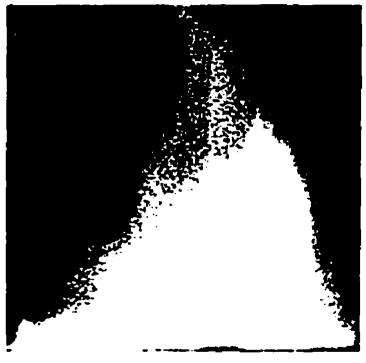

(b) shifted 3 mm

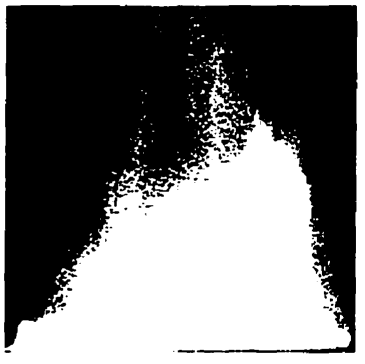

(c) shifted 5 mm

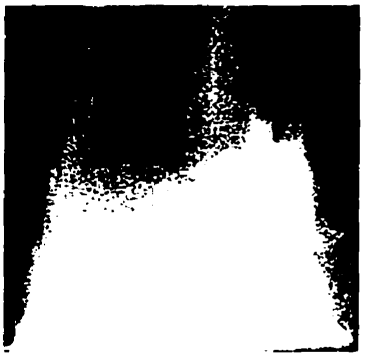

(d) shifted 10 mm

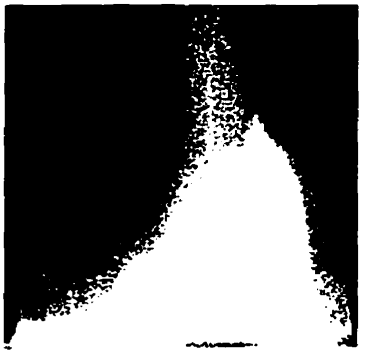

(e) rotated 3°

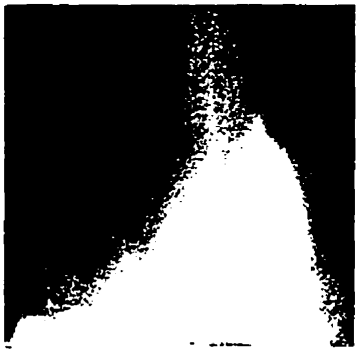

(f) rotated 5°

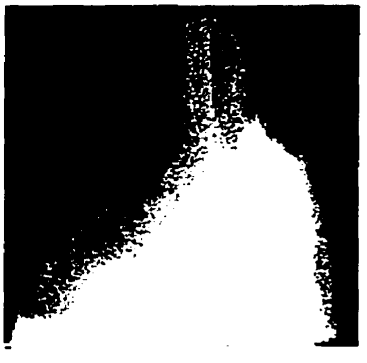

(g) rotated 10°

Figure 3.3: Feature space histogram and image misregistration in MR/tPET images. Due to the blurring of MRI (Gaussian kernel of $FWHM = 9mm$ was applied) and tPET (intrinsic blurring) images, the "cloud" in the feature histogram distributed widely.

the correlation value for a geometric transformation T on A is defined as:

$$corr(A, B; T) = \sum_{I}\sum_{J}\sum_{K} A \cdot T(B) \tag{3.3}$$

The transformation T is the solution for the registration problem if it maximizes the correlation value.

The matching feature used in these kind of methods can be voxel intensity [61], or derived features such as voxel intensity gradient [59, 60, 61], or ridge-like L_{vv} features [57]. However, in multimodality registration, directly using voxel intensity as the matching feature is less successful, because the voxel intensity values in one image are usually not a monotonic function of the voxel intensity values in the other image acquired from a different image modality. This leads to multiple values in one image corresponding to the same value in the other image.

3.4.3 Variance of Voxel Intensity Ratio Method

The variance of voxel intensity ratio method was first introduced by Woods et al. [15] to deal with the intra-subject intra-modality registration problem. The assumption behind this method is that the voxel intensity from the same tissue type from one modality should be the same, or only different by a constant factor. In other words, the ratio of voxel intensities from the image pair should be a constant when the two images are registered. However, in realities, even two exactly aligned images will show some residual variation due to counting statistics, partial volume effect, and interpolation error. Therefore, the similarity measurement for the registration is defined as the variance of this ratio. As an illustration, let a_i and b_i be the intensity of voxel i from the two images to be registered:

$$r_i = \frac{a_i}{b_i} \tag{3.4}$$

where i covers all possible voxels in the volumes.

And the normalized variance value can be represented:

$$R = \frac{r_\sigma}{r_m} \tag{3.5}$$

where r_σ is the standard deviation and r_m is the mean value of r_i. When the two images are registered, the variable r_i should be maximally uniform if not constant (when registering two images on the same subject and from the same modality), which minimizes the value R.

In intra-modality registration, the variance of the intensity ratio (**VR**) [15] method is based on the assumption that there is a linear relationship between the matching feature across the whole volume. However, in multi-modality image registration, this assumption does not hold, especially in the case where one volume is an anatomic image and the other is a functional image. Nevertheless, Woods et al. extended this idea to the multimodality image registration [63]. In this method, instead of using a global random variable r_i as in Equation 3.4, a set of such intensity ratios, based on the segmentation of the reference image, is used to overcome the non-linear relationship between voxel intensities across the two volumes in MRI/PET registration.

The reference image (the MR image in MRI/PET registration) is partitioned depending upon the intensity value. The voxels whose intensity values are equal to b_j are in the same partition j. A variable r_j is defined as:

$$r_j = \frac{a_j}{b_j} \tag{3.6}$$

where a_j are intensity values from corresponding voxels of the other image.

For each variable r_j, the same measurement R_j as in Equation 3.5 can be generated. Finally, the similarity measurement is defined as the weighted average of R_j:

$$R' = \sum_j \frac{R_j \times n_j}{N} \tag{3.7}$$

where n_j is the number of the voxel pairs in the partition j and the N is number

of whole voxel pairs in the registration ($N = \sum_j n_j$). When the two images are registered, R' should be minimized.

Woods et al. reported successful registration of MRI/PET images (PET FDG images) by this method, obtaining a mean 3-D error in the registration result of less than 2 mm [63].

In an adaptation of the Woods' approach, Hill et al. [81] proposed selecting specific bins of the intensity value from the feature space histogram to calculate the variance of the voxel intensity ratio in the MR/CT image registration. For each bin, different weights can be used on the variance ratio; i.e., more weights can be assigned to the bins corresponding to tissues that are likely to be useful for registration.

3.4.4 Mutual Information Method

In information theory, entropy is a measure of the uncertainty of a random variable and can be denoted as [71]:

$$H(X) = -\sum_{x \in X} p(x) log(p(x)) \tag{3.8}$$

where X is a random variable and p(x) is the probability mass function of X.

It is very easy to extend the entropy concept to a pair of random variables. Joint entropy H(X,Y) of a random variable pair (X,Y) is defined as:

$$H(X,Y) = -\sum_{x \in X} \sum_{y \in Y} p(x,y) log(p(x)p(y)) \tag{3.9}$$

where p(x), p(y) are the marginal probability distributions of X, Y respectively, and p(x,y) is the joint probability distribution of (X,Y).

Mutual information of random variables X and Y is introduced to measure of the amount of information that one variable contains about another variable:

$$I(X;Y) = \sum_{x \in X} \sum_{y \in Y} p(x,y) log[\frac{(p(x,y))}{p(x)p(y)}] \tag{3.10}$$

If one random variable contains more information about the other, the mutual information value will be higher due to the reduction in the uncertainty of one random

variable from the knowledge of the other. The relationship between the joint entropy and mutual information is:

$$I(X;Y) = H(X) + H(Y) - H(X,Y) \tag{3.11}$$

Based on these concepts, Collignon et al. recently proposed two voxel-based registration methods. First, they used the entropy of the joint probability distribution of the combined intensity values of all common voxel pairs in the two images as the similarity measurement [69]:

$$E(X,Y;T) = -\sum_{x\in X}\sum_{y\in Y} p(T(x),y)log(p(T(x))p(y)) \tag{3.12}$$

where X and Y are random variables that represent the voxel intensity from the source and the target volumes and T is a geometric transformation applied to the source volume. Ideally the transformation T is the registration result when it minimizes the function $E(X,Y;T)$.

In subsequent work [70], they found that the joint entropy measurement is sensitive to the problem of partial overlap of the two data sets. They then proposed using mutual information of the joint probability distribution to improve the robustness of the method to partial overlap and to reduce the number of local minima in the parameter searching space:

$$MI(X,Y;T) = -\sum_{x\in X}\sum_{y\in Y} p(T(x),y)log[\frac{p(T(x),y)}{p(T(x))p(y)}] \tag{3.13}$$

Again the registration result is the transformation T which can minimize $MI(X,Y;T)$.

The assumption behind these two methods is that when two related images correctly registered, one image should provide the most information about the other one, thereby minimizing $E(X,Y;T)$ or $MI(X,Y;T)$. The author didn't give quantitative evaluation of MRI/PET registration using this method, but their result from MRI/CT registration indicated that registration error is below 2.5 mm.

3.4.5 Discussion of Voxel-based Registration Methods

All of the voxel-based registration methods described above use a similarity measurement to solve the registration problem. Ideally, the measurement is maximized or minimized when the images are exactly registered, and it decreases or increases monotonically with increasing misregistration between the two images. Furthermore, the methods use all possible voxels in the two image volumes to calculate the similarity measurement. This has the advantage of robustness against random noise and the partial overlap problem.

Besides the three methods reviewed in this section, there are several other voxel-based methods, such as the methods based on measurement of *sum of absolute differences* [66, 67], *stochastic sign change* [12, 14], and *region overlapping* [68]. However these methods are either not suitable for the multimodality registration problem or they require user interaction during the registration procedure. These methods are not discussed here.

Although cross-correlation of voxel intensity is not suitable in the multimodality registration problem, it can be applied to derived features such as intensity gradient to accomplish the multimodality registration (such as MRI/CT registration [57]).

The variance of intensity ratio measurement in the MRI/PET registration problem requires that the regions corresponding to scalp and skull be removed before registration. The removal of these regions might increase the likelihood that all voxels with a particular value in the MRI study will represent similar tissue types [63] and thus reduce the number of local minima in the parameter searching space. This preprocessing step usually involves human intervention. At the Montreal Neurological Institute, the non-brain structures can be extracted automatically using a brain atlas in standard space. In this approach, the MR image is first re-sampled into the standard 3-D coordinate space of the atlas using 9-parameter transformation (3 rotations, 3 translations and 3 scales)[62]. The brain atlas can then be used as a mask to zero the extra-cerebral voxels in the image.

Information theory methods proposed by Collignon et al., are different from Woods' **VR** method in that the similarity measurement is symmetric. The **VR** method is not symmetric since the result depends upon which of the two images is used as the reference image. For example, in MRI/PET registration, the MR image is chosen as the reference image. In the information theory based methods, on the other hand, the selection of the reference image is not important, and this symmetric similarity measurement may lead a more robust registration method.

3.5 Summary

Multimodality image registration is a difficult problem in the medical imaging field. Although many methods have been proposed, there has been no consistent way (i.e., different methods were validated by using different data sets) to compare the registration accuracy and robustness among these methods from the literature. Therefore, it is also hard to choose the best from the existing methods. For practical use, the amount of human interaction, the computation efficiency of the method, and the data dependency of the method (i.e. a registration method may work well with MRI/CT image registration but not with MRI/PET) affect the selection of the registration techniques. Most attention in this review was paid to matching features and the similarity measurements of the registration methods; however, due to the complexity of the image registration problem, other elements in the registration algorithm may also affect the performances of the technique, such as the interpolation algorithm and the optimization method. These issues are discussed in Chapter 4 and 5.

Chapter 4

Registration and Validation Methods

Two registration methods were implemented for MRI/tPET image registration - Mutual Information (**MI**) and Variance of Intensity Ratio (**VR**). In this chapter the implementation details will be discussed first, followed by a description of the validation methods.

4.1 Introduction

In the implementation of MRI/tPET image registration, the higher resolution MR images are taken as source volumes and tPET images as target volumes. Therefore, once the registration result has been obtained, the MR image can be re-sampled by the geometric transformation into the coordinate space of the PET image in order to perform voxel-to-voxel comparisons.

Because of the rigid skull of the head and intra-subject characteristics of MRI/tPET image registration, the parameter searching space of this registration can be safely restricted to a set of global rigid body transformations, which have six degrees of freedom - three translations and three rotations. In order to facilitate the calculation

of the transformation, a homogeneous matrix is used:

$$\begin{pmatrix} x' \\ y' \\ z' \\ 1 \end{pmatrix} = RT \begin{pmatrix} x \\ y \\ z \\ 1 \end{pmatrix}. \tag{4.1}$$

where RT denotes the rigid body transformation; x', y', z' and x, y, z are the three dimensional coordinates of the transformed and original voxels respectively.

The rigid transformation can be decomposed into three translational and three rotational parameters as follows:

$$\begin{aligned} RT &= R \cdot T \\ R &= R_x \cdot R_y \cdot R_z \end{aligned} \tag{4.2}$$

where R is the rotation homogeneous matrix and T is the translation matrix. From this equation, it can be seen that the order of the matrices is not interchangeable for rigid body transformation. The three matrices R_x, R_y, R_z, and the translation matrix can be represented as:

$$R_x = \begin{pmatrix} 1 & 0 & 0 & 0 \\ 0 & \cos\theta & \sin\theta & 0 \\ 0 & -\sin\theta & \cos\theta & 0 \\ 0 & 0 & 0 & 1 \end{pmatrix}, R_y = \begin{pmatrix} \cos\phi & 0 & -\sin\phi & 0 \\ 0 & 1 & 0 & 0 \\ \sin\phi & 0 & \cos\phi & 0 \\ 0 & 0 & 0 & 1 \end{pmatrix}, R_z = \begin{pmatrix} \cos\varsigma & \sin\varsigma & 0 & 0 \\ -\sin\varsigma & \cos\varsigma & 0 & 0 \\ 0 & 0 & 1 & 0 \\ 0 & 0 & 0 & 1 \end{pmatrix}. \tag{4.3}$$

$$T = \begin{pmatrix} 1 & 0 & 0 & T_x \\ 0 & 1 & 0 & T_y \\ 0 & 0 & 1 & T_z \\ 0 & 0 & 0 & 1 \end{pmatrix} \tag{4.4}$$

where θ, ϕ, and ς are the counter-clockwise rotations about the x, y, and z axes respectively; and T_x, T_y and T_z are the translations along the x, y, and z axes respectively.

These matrices are concatenated into a single six-parameter homogeneous matrix:

$$RT = \begin{pmatrix} cos\phi cos\varphi & cos\phi sin\varphi & -sin\phi & T_x \\ sin\theta sin\phi cos\varphi - cos\theta sin\varphi & sin\theta sin\phi sin\varphi + cos\theta cos\varphi & sin\theta cos\phi & T_y \\ cos\theta sin\phi cos\varphi + sin\theta sin\varphi & cos\theta sin\phi \sin\varphi - sin\theta cos\varphi & cos\theta cos\phi & T_z \\ 0 & 0 & 0 & 1 \end{pmatrix} \quad (4.5)$$

4.2 Preprocessing the Source MRI Volume

Since the FOV of the MRI data usually covers the head and neck, which contains a much larger volume than the tPET image, it is necessary to crop the MRI data to cover approximately only the volume of the brain.

To make use of standard Talairach space to crop the MR image to the desired extent, two preprocessing steps are accomplished automatically with application tools already built at the BIC of MNI:

1. Transform the MRI data into the standard Talairach space [61] through the registration of MRI data to an average brain model [62].

2. Use the average brain volume in Talairach space to mask the undesirable volume in the original MRI data. The cropped rectangular volume encases the head from the top of the scalp to the middle of the cerebellum vertically.

4.3 Registration Methods

4.3.1 Estimation of Probability Distribution of Random Variables in the Mutual Information Method

The similarity measurement in the MI method (Equation 3.13) requires the knowledge of probability distributions of the random variables. The probability distribution is estimated from the observation of the feature histogram. Collignon et al. [70]

indicated that if the quantization of the feature space histogram is too fine, the application of Parzen-windowing [72] can be used to reduce the effect of image noise and increase the reliability of the estimation. However, the computation cost of this method is high. According to Collignon et. al. [70], it is expected that small intensity distortions of the observations do not introduce large deviations in the registration solution. Upon these, a crude but computational efficient approximation method - normalized feature space histogram - is used in our implementation. The normalized feature space histogram is defined as:

$$p(x, y) = \frac{h(x, y)}{N} \tag{4.6}$$

where $h(x, y)$ is the feature space histogram, and N is the number of voxel pairs in the overlapped sample set when calculating $h(x, y)$.

The marginal probability distributions of $p(x)$ and $p(y)$ are also estimated in a similar way. Since there might be different overlap between the two image volumes in each transformation during the optimization procedure, $p(x)$ and $p(y)$ are re-calculated for each transformation as well as $p(x, y)$.

4.3.2 Estimation of the Initial Transformation

The initial transformation of the registration procedure is usually important to the iterative registration algorithm in two aspects:

- A better estimation of the initial transformation which is closer to the correct registration transformation will save more computation time on the searching for the optimal transformation in the parameter hyperspace.
- A better estimation of the initial transformation will make the two images have larger overlapped volume, which can reduce the local minima in the parameter hyperspace in the voxel-based registration algorithm.

In our implementation, only the translation parameters are estimated for the initial transformation and all the rotation parameters are set to 0° at the beginning

of optimization procedure. Two methods for the estimation of initial translation parameters have been implemented:

- Take the translational alignment of the geometric centers of the volume (center coordinate of the image volume) of the two images as the estimation of initial translation parameters.
- Take the translational alignment of the centers of gravity (COG) of the two images as the estimation of initial translation parameters.

The comparison between the two approaches will be addressed in next chapter.

4.3.3 Multiresolution Registration Scheme

Owing to the low spatial resolution of the tPET image, high-resolution information in the MRI volume may not be useful and a sub-sampled version of the MRI image volume may be quite adequate for registration purposes while yielding faster results. However, combined with noise effect, subsampling the MRI data during calculation of the similarity measurement may cause more local minima in the parameter search space.

Woods et al. [63] used a hierarchical strategy in their **VR** method, which starts with sampling the source volume at every 81st voxel. The convergence transformation parameters at this stage are used as the initial parameters for the next stage where the sampling rate decreases to $27:1$. This procedure is repeated with ratios of $9:1$, $3:1$, and finally $1:1$. The intention of this hierarchical scheme is to:

- increase the chance of not being trapped by local minima in the parameter search space. Since a local minimum in one stage may not be a minimum in the next stage due to more information involved in the similarity measures, this scheme increases the possibility that the optimization procedure avoids being trapped in a local minimum and reaches the global minimum.

- accelerate the convergence of the searching procedure. Subsampling the source image volume greatly reduces the computation cost for the calculation of the similarity measurement.

Studholme et al. [65] used a traditional low-pass pyramid representation of the image [74, 75] to achieve multiresolution optimization. In their algorithm, multiple resolution versions of images are created by averaging neighboring voxels. For an example, the optimization procedure starts at the top of the pyramid, where the image is built by averaging each $8 \times 8 \times 8$ neighboring voxels. The registration result at this level is taken as the initial guess of the registration at the next level where the image is a less blurred version of the original, created by averaging $4 \times 4 \times 4$ neighboring voxels. This procedure repeats until the original resolution.

In our implementation, we also use a hierarchical multi-resolution strategy to optimize the similarity measurement with two important differences from the other methods described above:

- The same sub-sampling interval is used in each of the x, y, and z direction.
- An isotropic 3D gaussian kernel is convolved with the MR image before registration.

Subsampling the source volume reduces the number of voxels involved in the calculation of 2-D feature space histogram, which in turn might increase the effect of the noise on similarity measurement. The Gaussian blurring kernel which is a linear-, shift-, and rotationally-invariant operator [61] [73], is able to reduce the number of local minima in the parameter searching space caused by the combination of noise and subsampling.

The multi-resolution scheme of our implementation begins with subsampling blurred MRI data at a sampling rate of $3:1$ in each of the x, y, and z direction, then performs a few iterations with a sampling rate of $2:1$ on MRI data to improve the registration

accuracy. The issue of selecting the starting and ending sampling rate for the multi-resolution scheme will be discussed later in Chapter 5. Compared with full sampling of MRI data, the sampling rate of $3:1$ and $2:1$ reduces the computation time to $\frac{1}{27}$ and $\frac{1}{8}$ respectively in one transformation during the optimization procedure.

4.3.4 Interpolation Methods

During the registration procedure, each voxel from the source volume has to be transformed into the coordinate space of the target volume. Due to the continuous characteristics of the transformation parameters and different voxel sizes between the source and the target volumes, the transformed voxel is generally not located at a grid point of the target image. Therefore, an interpolation algorithm must be applied to the source image to obtain an interpolated voxel intensity value at each grid point of the target volume.

The simplest interpolation method is the nearest neighbor interpolation, in which the value at the interpolation point is assigned to the value of the voxel that is closest to the interpolation point. The advantage of this method is its efficiency. However, the nearest neighbor interpolation may cause the whole image to be shifted with regard to the intended position. Sub-voxel interpolation accuracy cannot be achieved by this method.

A better interpolation method is linear interpolation (trilinear in 3-D) where the value of the interpolation point is obtained by linearly interpolating neighboring points. The linear interpolation may result in smoothing of the image [76].

In the **MI** method, applying the trilinear interpolation method on the target image may cause unpredictable changes of probability distribution $p(y)$ [70]. Thus Collignon et al. [70] proposed a method called trilinear partial volume distribution interpolation. Instead of using the interpolation weights to average the neighboring voxels in the target image as in trilinear interpolation, Collignon's method distributes the same interpolation weights onto the corresponding neighboring voxels in the target

image when calculating the feature space histogram (scatter plot). In this way, the normalized histogram of the target image, which is the estimation on the probability distribution of $p(y)$, will not change discretely by the interpolation operation.

Finally, a higher order interpolation method - tricubic interpolation, has been implemented with the registration algorithm. This method involves a $4 \times 4 \times 4$ instead of $2 \times 2 \times 2$ neighborhood of voxels around the interpolating point, giving it the attribute of continuous second order derivative. Although the tricubic interpolation method leads to more accurate and smoother estimation of the value between the image grid than the other three methods, its computation cost is much higher (i.e. at least it will take six times more than the trilinear interpolation method to obtain a interpolation value), because of the greater number of voxels involved in the calculation.

4.3.5 Optimization Method

The optimization method is an important element of the registration algorithm. A good optimization method usually can be characterized by the following three characteristics:

- the ability to converge in any condition;
- the ability to converge quickly;
- the ability to escape from local minima/maxima and finally to converge at a global minimum/maxima.

However, in practice it is not easy to find a method that meets all of these requirements. For instance, the so-called global optimization methods, such as simulated annealing [78] and the genetic algorithm [79], are able to avoid being trapped by local minima, but they are not computationally efficient.

In 3-D medical image registration, the number of optimization parameters is usually six or more. The multivariate characteristic of the optimization in medical image registration dramatically increases the complexity of the problem.

Various optimization methods have been incorporated into the multimodality image registration algorithms. Woods et al. [63] used the Newton-Raphson algorithm [80] which takes advantage of the easily obtained true derivative value of the similarity measurement. Collins et al. [61] implemented the Simplex optimization algorithm [80] in their MRI-MRI intersubject registration algorithm, which is a downhill method that does not require derivative information and has some resilience to local minima. Collignon et al. [70] used the Powell algorithm [80] to minimize the mutual information similarity measurement. Due to the efficiency of the downhill methods, which stop when they reach an extrema regardless whether the extrema is global or local, they have been used in many 3-D medical image registration methods. However, to reduce the effect of local extrema within the parameter searching space, several approaches have been proposed to improve these original optimization algorithms:

- Multi-start approach [81]. In this approach, many initial guesses of the solution are used to start the optimization algorithm hoping that one of the starts can lead to the global minimum.

- Multi-resolution structure of the optimization algorithm [61] [63] [65]. In this method, the registration starts with lower resolution image volumes, then the result of this stage is used as the initial guess for the next stage where higher resolution images are matched. Using this approach, the iterative searching procedure have better chance to avoid being trapped by the local minima in the parameter search space.

- Better estimation of initial transformation. This will give the optimization a much better chance to get to the global minimum. Collins et al. [61] used the principle axis transformation registration method [19] to get an initial estimation of the desired transformation.

In our implementation of both **MI** and **VR** methods, an improved version of the Powell method [82, 83] with multi-resolution structure was chosen as the optimization

method. In this method, whenever the optimization method reaches a minimum (either global or local), it will not stop but apply a random perturbation (translations within ± 3 voxels and rotations within $\pm 1^{\circ}$) to the transformation parameters. If the optimization procedure moves back to that minimum position after the perturbation, the optimization will finally stop. Otherwise, it will take that minimum as a local one and resume searching in the parameter hyperspace until the global minimum is reached or an iteration limit is imposed. Along with the multi-resolution strategy, the perturbation applied to the transformation parameters increases the possibility that the algorithm is not trapped by local minima.

4.3.6 Structure of the Implementation

It is desirable that the implementation be modular so that different elements of image registration may be easily plugged into the algorithm (see Figure 4.1). For example, the similarity measurement function of the registration can be changed among the **MI**, **VR**, or other new similarity functions. Thus, the structure of our implementation clearly separates three major elements from each other, and strictly defines the interface of these three elements:

- Similarity measurement function - **MI** and **VR** are supported by the current version of the program.
- Interpolation method - nearest-neighbor, trilinear, tricubic and trilinear partial volume distribution interpolation methods are supported.
- Optimization method - only the Powell method is currently supported.

This modular implementation structure enables the program to easily extend the current method for a specific element while keeping others unchanged. Furthermore, it is also useful for investigation of the performance of different methods, such as the comparison of the performances between the **MI** and **VR** methods.

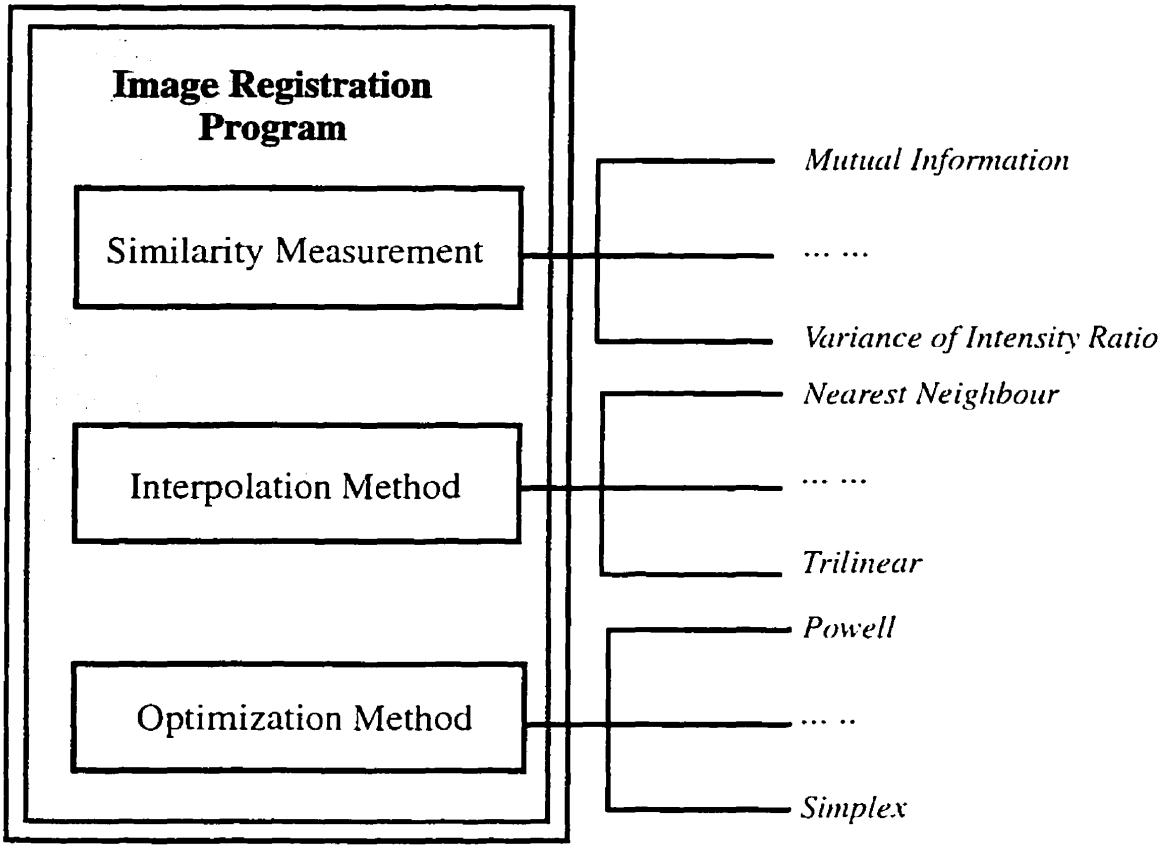

Figure 4.1: Implementation Structure

4.4 Validation Methods

Validation of a registration algorithm in medical image registration itself is not trivial, since the true registration solution is unknown for real images.

Several methods have been proposed to validate medical image registration algorithms. They can be classified into three categories:

- Visual inspection of the superimposition of the re-sampled source image and the target image [84]. This method is subjective and non-quantitative, hence it is not suitable for an accurate comparison between different algorithms. However, this method does not require any special procedure during image acquisitions and it enables a quick assessment on the success of the registration algorithm.

- Use the registration result from the extrinsic landmark-based registration method as a reference to validate the registration algorithm [19, 63]. The comparison of the registration result with the reference transformation can give a quantitative evaluation of the registration error. However, the reference transformation might also contain misregistration, for instance, the extrinsic markers may move between scans.

- Use simulation data for validation [85]. There are two advantages to use simulation data to validate image registration:

  - The true registration result is known exactly, which enables the quantitative measurement of misregistration;
  - The simulation program can generate image data with different scanning settings. Thus the validation can be performed on image data with various resolutions, noises, and contrast. It is useful to test the robustness of the registration method against these factors.

In this thesis, both visual inspection method on real data and quantitative validation on simulated tPET data (details escribed in Chapter 5) are used to validate

the MRI/tPET image registration algorithms.

4.4.1 Quantitative Measurement of Misregistration

The validation method used on MRI/tPET data registration proceeds with the following steps:

1. Using a 3-D MRI data set as input to the PET simulator (which will be described in next chapter), generate a tPET image volume.

2. Generate a random rigid body transformation T_r, in which the translations are within range of ± 10 mm and the rotations are within the range of $\pm 10°$. The rotations are centered on the geometric center of the image volume.

3. Use the generated random transformation to re-sample the MRI data, which yields a MR image no longer spatially aligned with the tPET image.

4. Apply the registration method on the transformed MR and simulated tPET images to obtain an estimated geometric transformation T_e.

5. Compare the result of registration algorithm T_e with T_r. Ideally, if the registration can recover the random transformation applied to the original MR image, T_e should be the inverse of the random transformation T_r.

To quantitatively measure the misregistration, it is desirable to use a single numerical value to represent the registration error. Since the rigid transformation contains translations and rotations, it is not suitable to combine them both into a single quantitative measurement error directly. Therefore, the quantitative measurement of misregistration is based on r.m.s. (root mean square) of the 3-D distance between two sets corresponding voxels in original MRI and the recovered MRI data sets. A set of voxels (P_i, $i = 1....N$) are chosen from the original MRI data. Then the random transformation T_r is applied to this set of voxels to different coordinates (P_i',

$i = 1....N$). The registration result T_e transforms the P_i' back to P_i''. If the $T_e = T_r^{-1}$, the 3-D distance σ between corresponding voxels from the sets P_i and P_i'' is zero. The value of σ can be represented as:

$$\sigma = \sqrt{\frac{\sum_i (P_i - P_i'')^2}{n}} \tag{4.7}$$

where $P_i'' = P_i * T_r * T_e$ and n is the number of points.

The same seven voxels as those chosen by Neelin et. al. [77] were used to evaluate the misregistration. The points were:

- the center of the brain.
- six voxels at 75 mm ($\approx$ radius of the brain) away from the centroid of the brain along each direction.

4.4.2 Similarity Measurement As a Function of Translational Misregistration

In order to qualitatively evaluate the performances of some implementation parameters such as sampling interval, function curves for the similarity measurement versus translational misregistration can be generated. This is accomplished by shifting the MR image t mm along one of the x, y, and z direction. The similarity measurement value can be calculated on the translated MR image and the corresponding simulated tPET image. Ideally, with $t = 0$ mm, the value should be minimized; while with t increasing, the MI value should increase monotonically also. Although the three curves can not fully reflect the parameter searching space, the smoothness of the curves and the number of local minima appearing along the curves indicate how well the implementation behaves for a specific similarity measurement. It should be noted, this qualitative evaluation does not cover the whole parameter searching space, i.e. "similarity measurement as a function of rotational misregistration" is not measured.

This is because the objective of this evaluation is qualitative and for comparison of the effects of different implementation parameters.

Chapter 5

Experiments and Results

In this chapter, experiments using the two registration algorithms (**MI** and **VR**) on MRI with simulated and real tPET images are presented. The first section describes the experimental data sets of MRI and tPET images. The next two sections present the results from the experiments on MRI/simulated tPET image registration and MRI/real tPET image registration respectively. The last section discusses the experiment results and compares the two registration algorithms.

5.1 Experimental Data Sets and Methods

This section describes the data sets and methods used in MRI/tPET registration experiments using both simulated and real tPET images.

5.1.1 MRI/Simulated tPET Image Registration

5.1.1.1 Experimental Data Sets

In order to quantitatively evaluate the image registration algorithms discussed in Chapter 4, two subjects were selected to acquire the experimental MRI/simulated tPET image data sets. The procedure of obtaining the MRI data and the simulated

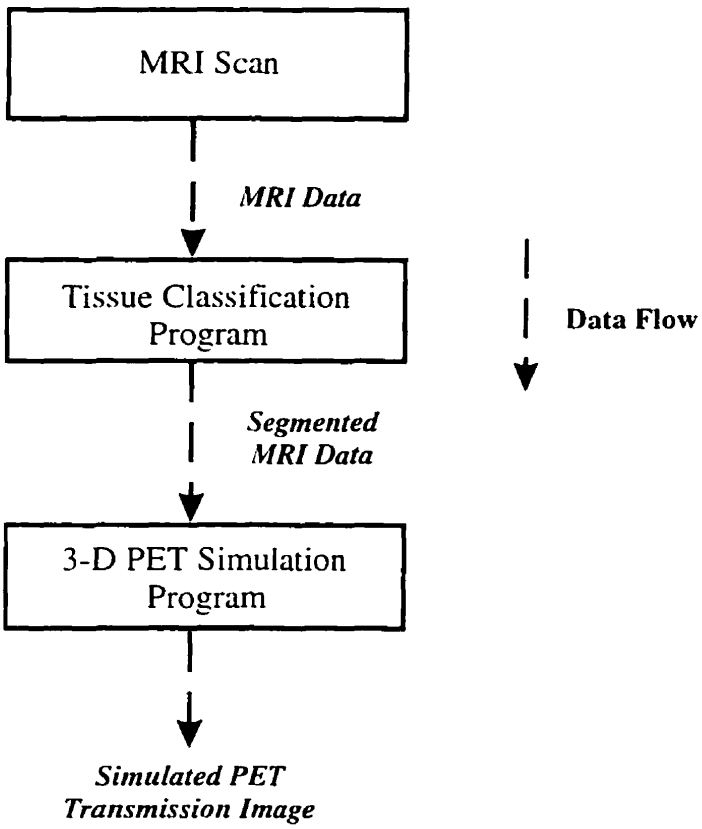

Figure 5.1: PET simulation procedure

tPET images is illustrated as in Figure 5.1.

In the first step, T1-weighted MRI data from the two subjects, S1 and S2, were collected on a Philips Gyroscan 1.5 Tesla system with 3-D gradient echo acquisition ($T_R = 75ms$, $T_E = 14ms$, flip angle = 60°, voxel size = $1 \times 1 \times 3$ mm^3). The two columns in Figure 5.2 show the sagittal slices of the two MR images and various blurred versions (blurred with different filter widths) of these two images respectively. As described in Chapter 4, two preprocessing steps were completed on the MR images - the images were re-sampled to have isotropic voxel size of $1 \times 1 \times 1$ mm^3 and cropped to cover only the brain.

An automatic tissue classification program was then used to segment the raw MRI

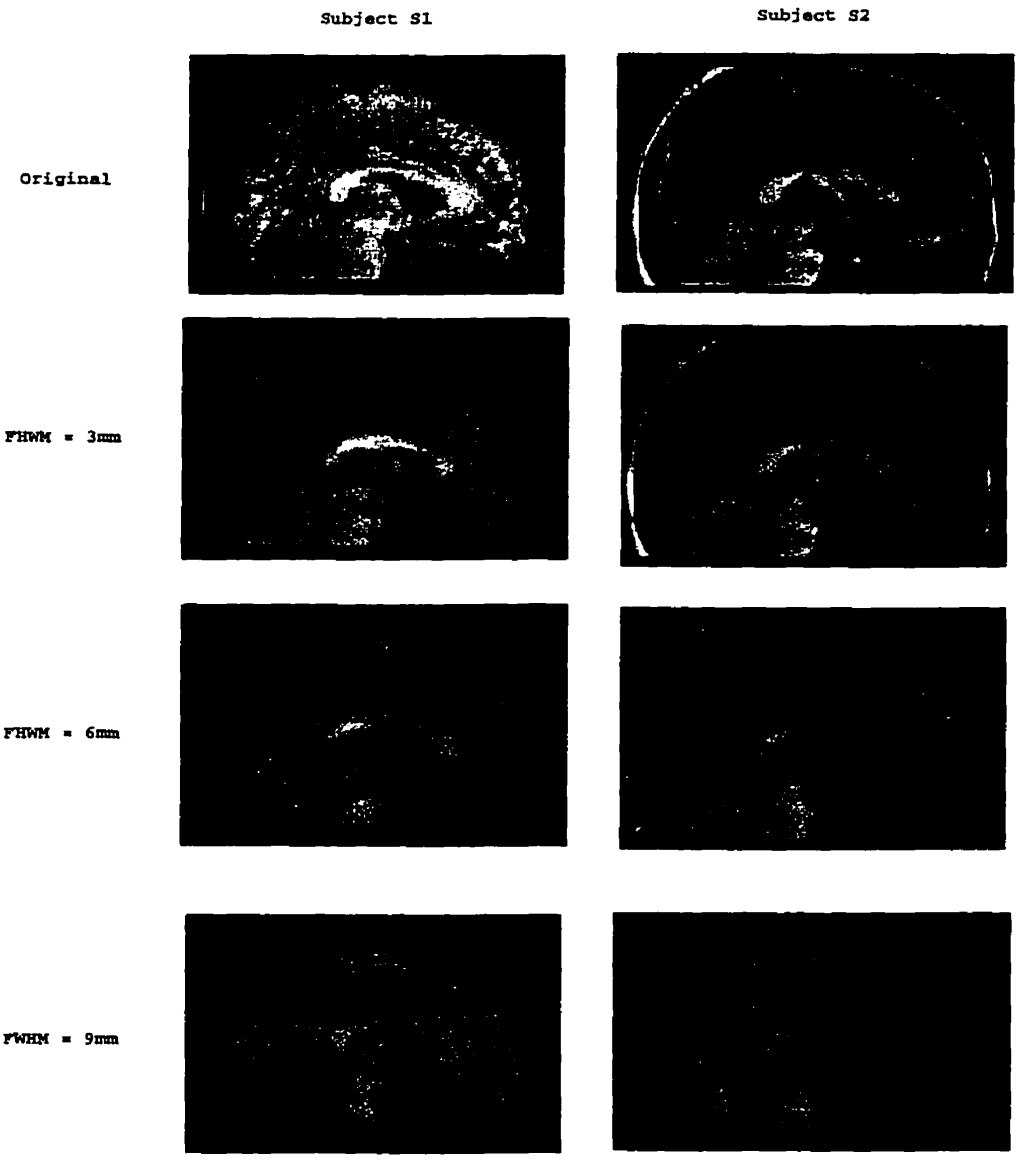

Figure 5.2: Sagittal slices of original MR images and the corresponding blurred MR images. The original MRI data were collected on a Philips Gyroscan 1.5 Tesla system. The slices shown here have been re-sampled and cropped. The blurred MR images were generated by filtering the original two MR images with a 3-D Gaussian kernel with FWHM = 3 mm, 6 mm, and 9 mm respectively.

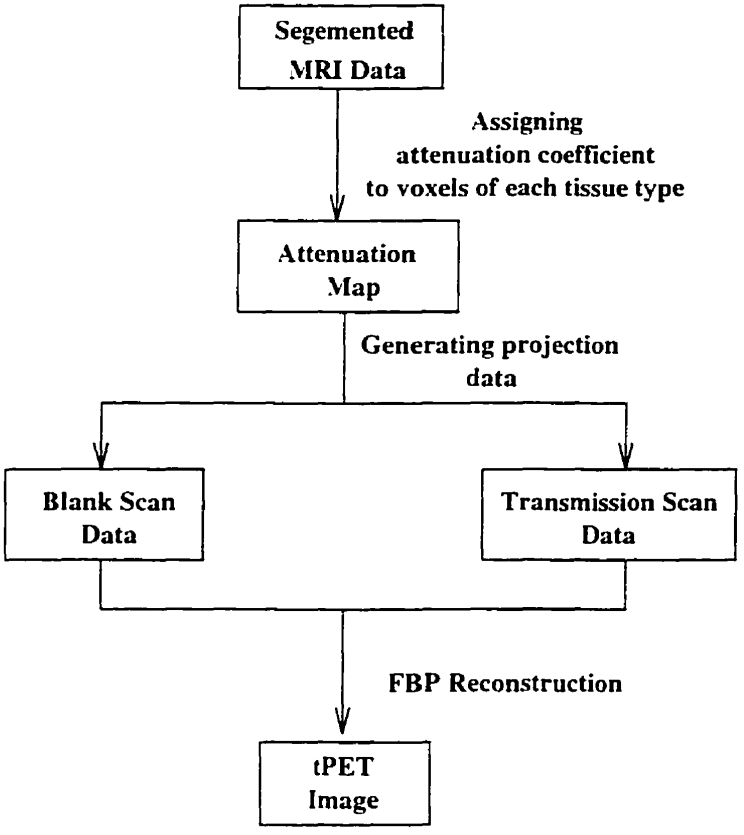

Figure 5.3: The procedure of a 3-D simulation program to generate tPET images.

data into gray matter, white matter, CSF structures, skull bone, scalp, and sinus [86, 87]. This segmented MR image is taken as a 3-D brain model. Using this model, a 3-D simulation program based on the geometry of the Scanditronix PC-2048 PET scanner [88, 89] was used to generate realistic simulated tPET image as illustrated in Figure 5.3. In the first step, the 3-D simulation program takes the segmented MRI data as input to create tissue attenuation maps by assigning the known attenuation coefficient at 511 keV to the voxels of each tissue type. Then, based on the physical design of the Scanditronix PC-2048 PET scanner system, the simulator incorporates the key physical characteristics of 3-D sampling and resolution, detector efficiency, attenuation, and count statistics, to generate realistic projection data. The simulation matches the configuration of the Scanditronix PC-2048 PET scanner, which generates tPET images with 15 slices, 6 mm slice thickness and 6.5 mm slice separation. The details of generating noisy blank and transmission scan data are as follows [89]:

1. The 3-D brain model image is resampled at specified image planes and smoothed with the axial resolution function of the scanner (i.e. Gaussian filter with filter width = 6 mm).

2. True counts and attenuation factors are calculated by projecting each image plane and corresponding attenuation map onto a uniform grid at all angular positions of the scanner (i.e. number of angles = 128, number of rays = 128, ray spacing = 2 mm). The projections counts are smoothed by convolving with the in-plane resolution function (i.e. Gaussian filter with filter width = 6 mm). Then they are mapped onto each detector position and adjusted by detection efficiency from the Scanditronix PC-2048 PET scanner system.

3. Scatter counts are estimated by convolving the projection with spatially variant filter derived from line source scans in water.

4. Random counts are estimated from measured single rates and scaled to give the desired total random counts. Noisy projection data are then generated from

Possion distributions with variance equal to the total counts.

In the last step, as in clinical studies, blank and transmission scan data were smoothed with a Gaussian filter (i.e. filter widths from 5 mm and 10 mm are used in this thesis) and reconstructed into transmission images by filtered backprojection. Figure 5.4 shows the central transverse slice of MRI and segmented MRI of subject S2. Figure 5.5 shows transverse slices of a real and a simulated tPET image.

In the following experiments, 12 tPET images (15 slices with 3-D voxel size = $2 \times 2 \times 6.5$ mm^3) were generated for each MRI volume from the two subjects (S1 and S2 as shown in Figure 5.2). These tPET images have three different resolutions (FWHM) and four different noise levels (maximum total counts per slice N_{max}) as listed in Table 5.1. Among these, image I_{23} (FWHM = 11.7 mm and $N_{max} = 9M$) closely matches the scanning conditions used in clinical studies. Figure 5.6 shows the sagittal slices of six (I_{11}, I_{21}, I_{31}, I_{13}, I_{23}, I_{33}) simulated tPET images of subject S1. The resolution of FWHM = 7.8 mm is the highest possible resolution for Scanditronix PC-2048 PET scanner used in clinical studies, therefore no higher resolution than FWHM = 7.8 mm was used in this thesis.

	$N_{max} = 0.9M$	$N_{max} = 2M$	$N_{max} = 9M$	$N_{max} = 28M$
FWHM = 7.8 mm	I_{11}	I_{12}	I_{13}	I_{14}
FWHM = 11.7 mm	I_{21}	I_{22}	I_{23}	I_{24}
FWHM = 16.2 mm	I_{31}	I_{32}	I_{33}	I_{34}

Table 5.1: Parameters of twelve simulated tPET images for each subject.

5.1.1.2 Experimental Methods

Based on the these simulated tPET images, two types of experiments were carried out in order to examine how different implementation parameters affect the registration algorithms and the performance of the registration algorithms under various

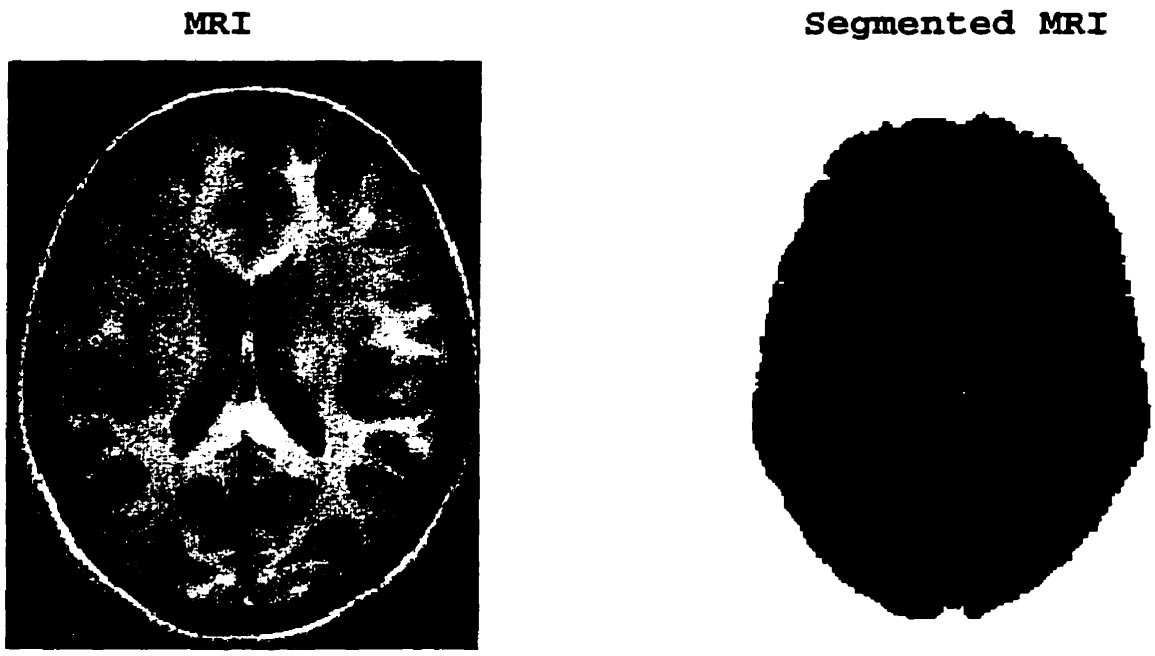

Figure 5.4: Central transverse slice of MRI and corresponding segmented MRI of subject S2.

conditions (i.e. different resolutions and noise levels):

A. Registration accuracy: A set of random transformations (translations within ± 10 mm, rotations within $\pm 10^{\circ}$) were applied the MRI data. The registration algorithm was then used to recover the MRI data from each of these transformations. The 3-D misregistration error was then measured by Equation 4.7 for each transformation. The mean of the r.m.s. values (r.m.s. value for each registration) was calculated for the whole trial as a measurement of the registration accuracy. The variance of the r.m.s. values for the trial was taken as an indication of stability of the registration algorithm.

B. Parameter sensitivity: Curves of similarity measurement as a function of translational misregistration were generated for each of the x, y, and z direction (As described in Chapter 4).

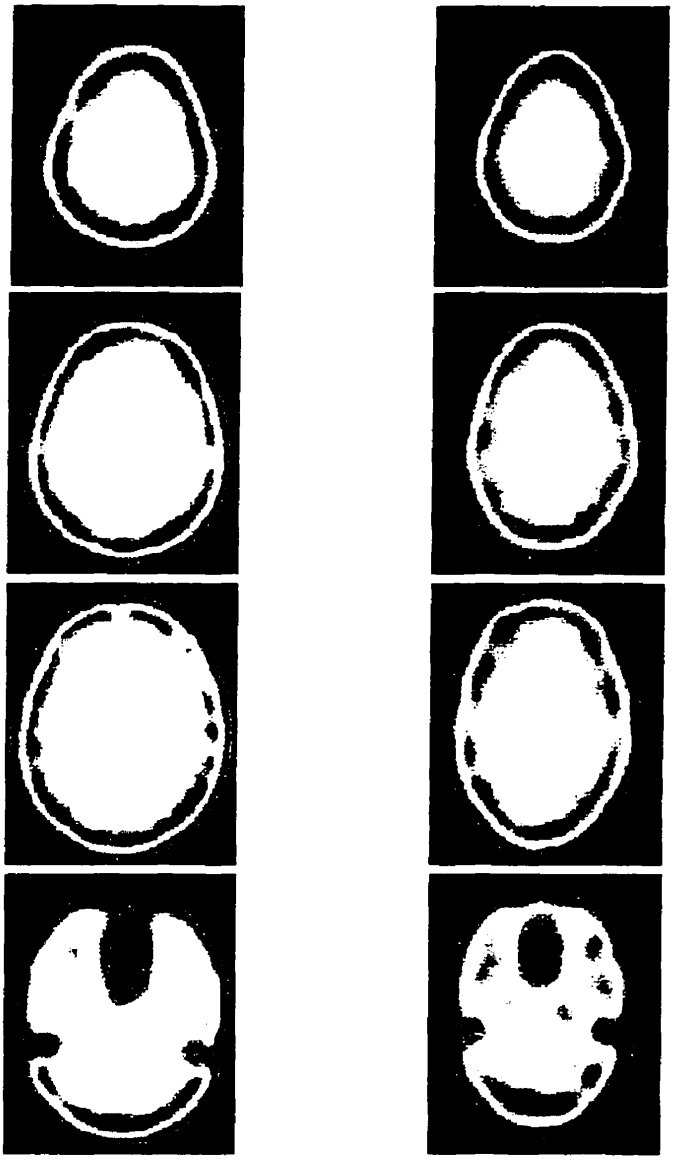

Figure 5.5: Simulated and real tPET images. The left column are transverse slices of simulated tPET image of subject S2 (with resolution FWHM= 11.7mm, maximum total counts in one slice = 9M). The right column are transverse slices of a typical real tPET from a different subject acquired from the Scanditronix PC-2048 at resolution of FWHM = 12mm. For each column, from top to bottom rows are transverse slices from top to bottom of brain in the tPET image volumes.

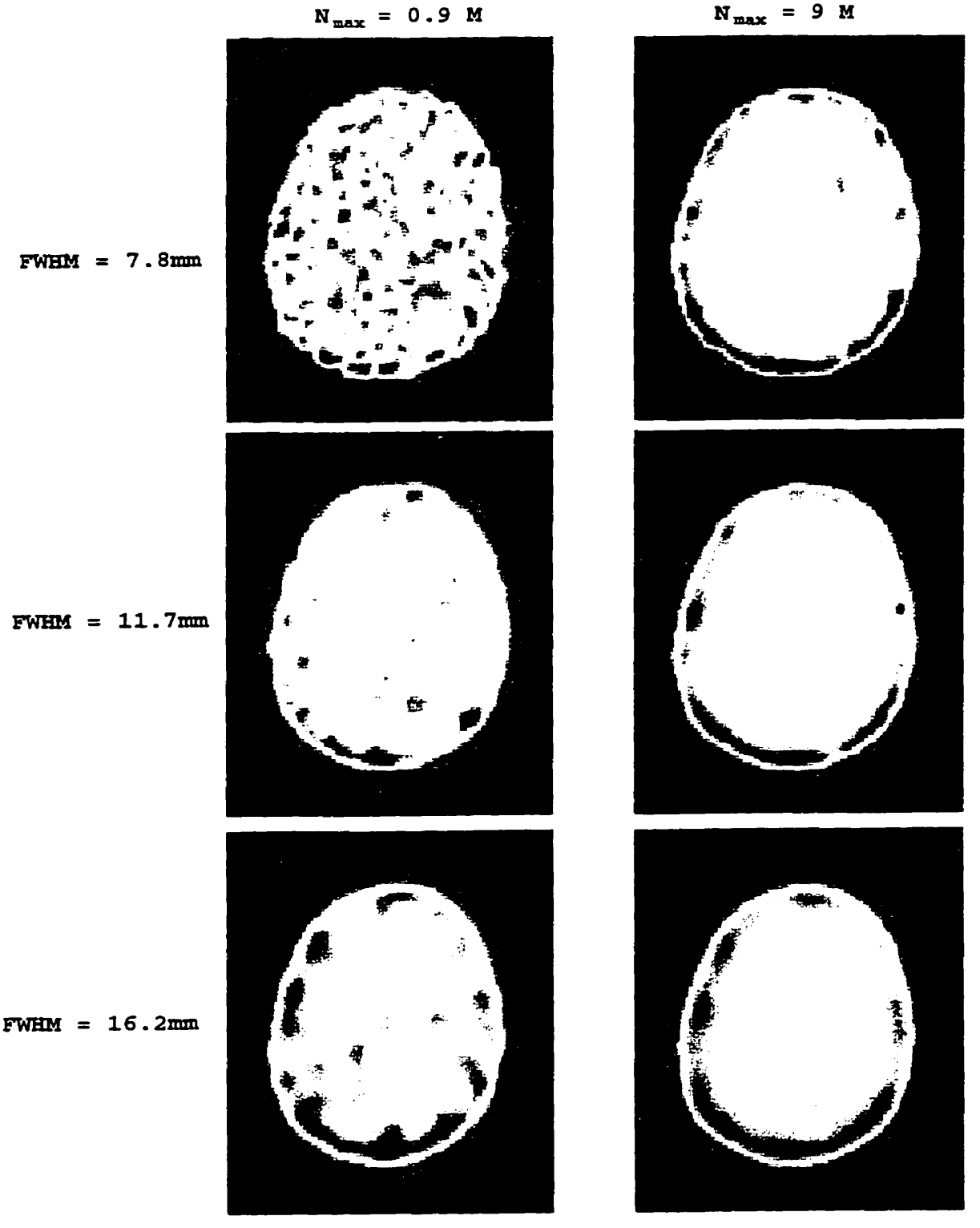

Figure 5.6: Simulated PET transmission images at different resolutions and noise levels from subject S1.

5.1.2 Real MRI and tPET Images

Although the true result of registration of MRI/tPET data is unknown and quantitative analysis of registration is not possible, it is important to apply the registration algorithms to real clinical data and visually inspect the registration error. This will highlight any gross errors which may not be apparent if the simulations do not adequately reflect the real situation.

5.1.2.1 Experimental Data Sets

Twenty-one T1 MRI data sets were collected from a Philips Gyroscan 1.5 Tesla system with a 3-D gradient echo acquisition (T_R = 18 ms, T_E = 10 ms, flip angle = 30°, voxel size = $1 \times 1 \times 1$ mm^3).

The tPET data sets from the same subjects were also acquired with a rotating Ge-68 rod source. Fifteen image volumes were collected with a Scanditronix PC-2048 (FWHM =20 mm, 15 slices and voxel size = $2 \times 2 \times 6.5$ mm^3). The other six tPET data sets were collected on a Siemens ECAT HR+ scanner (FWHM = 8 mm, voxel size = $2 \times 2 \times 2.4$ mm^3 with 63 slices), which can generate images with a larger FOV and better spatial resolution than the Scanditronix PC-2048 tomograph.

5.1.2.2 Experiment Method

The experiments performed on real data focused on testing if the **MI** algorithm (**VR** method was not used on real data sets, refer to Section 5.3 for the details) could succeed in the registration of real MRI/tPET images. The MRI data were first blurred with an isotropic 3-D Gaussian kernel with FWHM = 6 mm (the choice of filter width will be discussed in Section 5.4.1.2), then cropped to cover only the brain approximately as described in Chapter 4. The registration algorithm was applied to all 21 subjects to register the MRI to the tPET images. Once the registration results were obtained, the MRI data were re-sampled using the transformation from the registration procedure, into the PET space and voxel-to-voxel comparison were performed.

The re-sampled MR and tPET images were superimposed and the registration error visually evaluated.

5.2 Results from the Experiments on MRI/Simulated tPET Images

Two sets of experiments performed on MRI/Simulated tPET images are described. We first examined how different implementation parameters would affect the performances of the voxel-based registration method. However, only the MI registration algorithm was examined and the subsequent experiments on both VR and MI methods used the same implementation parameter settings derived from this experiment (the choice of the implementation parameters for VR method will be addressed in Section 5.2.2). The second set experiments evaluated the performances of both the MI and VR registration algorithms using four criteria:

1. registration accuracy
2. stability against noise
3. stability against spatial resolution
4. robustness to data truncation.

5.2.1 Implementation Parameters

Three issues were examined in this set of experiments:

1. method of estimation of the initial transformation:
2. subsampling interval and blurring filter width:
3. interpolation method.

All of the experiments here were focused on the **MI** method. In the second set of experiments (Section 5.2.2), both the **MI** and **VR** methods used the same implementation parameter settings (see Section 5.2.2 for details).

5.2.1.1 Estimation of the Initial Transformation

Two trials of experiment type A (registration accuracy, see Section 5.1.1.2) were applied to MRI and simulated tPET image I_{23} (FWHM = 11.7 mm, $N_{max} = 9M$) from both subjects S1 and S2. Each trial included 20 random transformations and the **MI** algorithm started with two different estimations of the initial transformation. The 3-D registration errors (Equation 4.7) showed that there is no big performance difference of the two methods on subject S1. This is because that the COG and geometric volume center of subject S1 are very close. But for subject S2 (there is a large offset between COG and geometric volume center for this subject), with an estimation of initial transformation by alignment of the image volume centers, two out of twenty (10%) tests failed (r.m.s. > 5 mm) while all the cases succeeded (r.m.s. < 2.5 mm) when an estimation by aligning COG was used. Furthermore, COG alignment reduced the number of iterations by typically 25% on average compared with volume center alignment.

5.2.1.2 Subsampling and Blurring on MRI

To investigate the effect of subsampling and blurring on MRI data, two trials of experiment type B (parameter sensitivity, see Section 5.1.1.2) were performed on MRI and simulated tPET image I_{23} from subject S1 and S2.

Figure 5.7 shows the **MI** function curves versus translational misregistration for subject S1 (similar curves were observed for S2) when the original and blurred MRI data were subsampled at sampling rate of 1 : 1 and 3 : 1 respectively. In the case of sampling rate = 3 : 1, the **MI** function curves for blurred MRI/tPET images have fewer local minima than those for non-blurred MRI/tPET images. When sampling

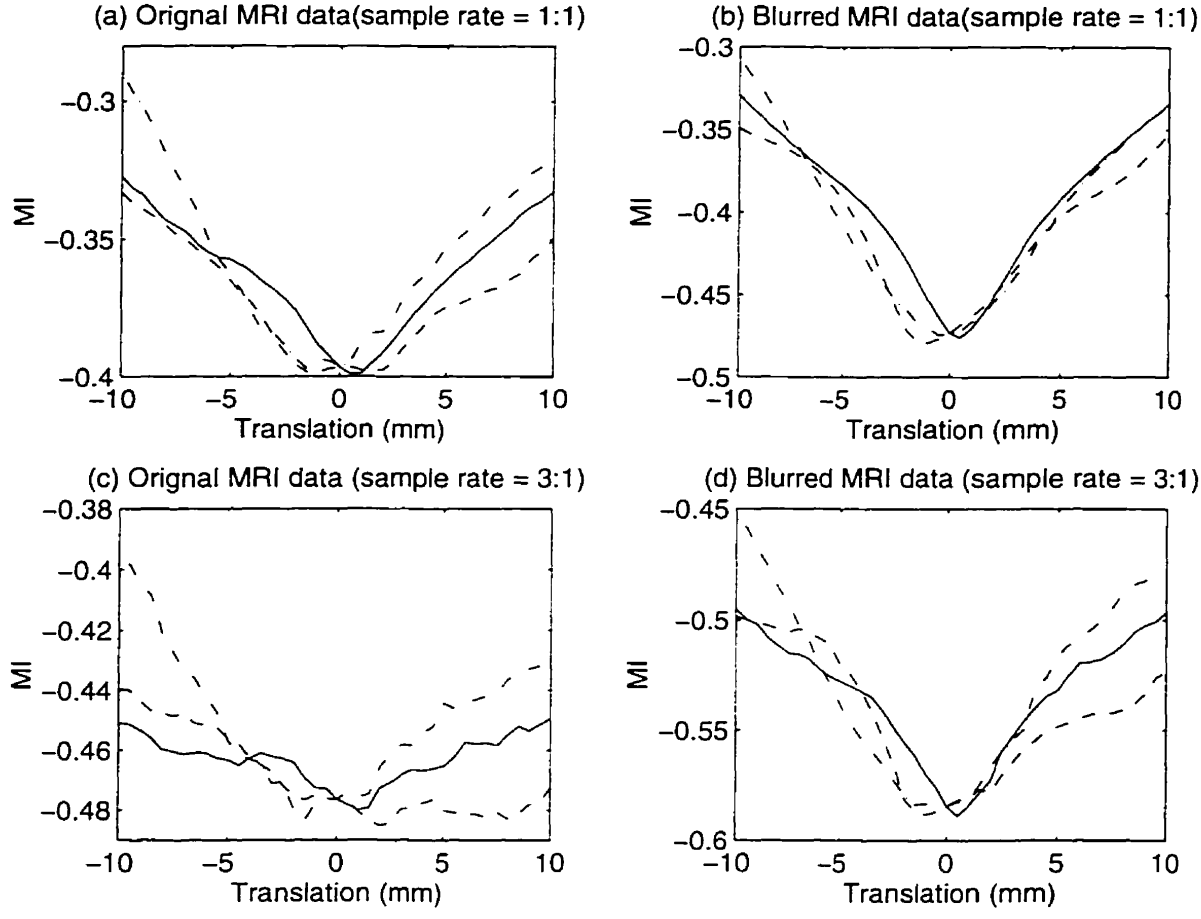

Figure 5.7: The **MI** measurement as a function of translations along the x, y, and z directions. Solid line - along x direction, dashed line - along y direction, dash-dot - along z direction. (a), (c) - the original MRI data subsampled with sampling rate = 1 : 1 and 3 : 1 respectively. (b), (d) the blurred MRI data (FWHM = 3 mm) subsampled with sampling rate = 1 : 1 and 3 : 1 respectively.

MRI data at full resolution, the **MI**-translational misregistration function curves for original MRI data do not have as many local minima as those at the sampling rate = 3 : 1. Nevertheless, they are still flat around the correct registration position and the local minimum in the curve for the y direction (anterior-posterior, dashed line in Figure 5) can be seen clearly. The Gaussian blurred MRI data, however, gives a sharper response around the correct registration position.

Figure 5.8 shows the **MI** versus translational misregistration function curves generated for the cases of subsampled blurred MRI data (FWHM = 3 mm and FWHM = 4 mm) at 1 : 1, 2 : 1, 3 : 1, and 4 : 1 rates. It can be seen from the figures that the shape of the curves obtained at the sampling rates 1 : 1, 2 : 1, and 3 : 1 are similar, without local minimum. The curves from sampling rate 4 : 1 has some local minima, especially when the MR image was blurred by the Gaussian kernel of FWHM = 3 mm, which is smaller than the sampling interval. For this reason, our implementation uses 3 : 1 and 2 : 1 as the starting and the ending sampling rates in the optimization procedure. The similar curves as FWHM = 4 mm, were observed for higher FWHM (i.e. FWHM = 6 mm and 9 mm), i.e. less local minima with sampling rate of 4 : 1 than the curves generated from FWHM = 3 mm.

For tPET data at various resolutions, there should be an optimal FWHM for the 3-D Gaussian kernel applied to the MRI data which yields the best registration performance. This issue was investigated by experiment type A using MRI at five resolutions (Gaussian kernel FWHM = 0 mm, 3 mm, 6 mm, 9 mm, and 12 mm) and simulated tPET images I_{13}, I_{23}, and I_{33} respectively from both subject S1 and S2.

Figure 5.9 shows the mean 3-D r.m.s. misregistration errors for this experiment. Consistent with the **MI** versus translational misregistration function curves in Figure 5.8, it can been seen that with the lowest resolution tPET image (FWHM = 16.2 mm), the procedure cannot recover the non-blurred original MRI data (FWHM=0 mm) from the random transformation very well due to unmatched information contained in MRI and tPET images (i.e. lack of details in tPET image but many details in non-blurred MR image). And for the tPET images at the medium resolution (FWHM = 7.8 mm and 11.7 mm), the **MI** algorithm is not very sensitive to the resolution of MR images; e.g., FWHM = 3 mm to 9 mm gave similar results. It can be noticed that the two subjects respond to the resolution of MRI differently, i.e., S1 shows a minimum at FWHM = 6mm with larger registration error at lowest resolution (FWHM = 12 mm) while S2 does not, this issue will be discussed later in Section 5.4.1.2.

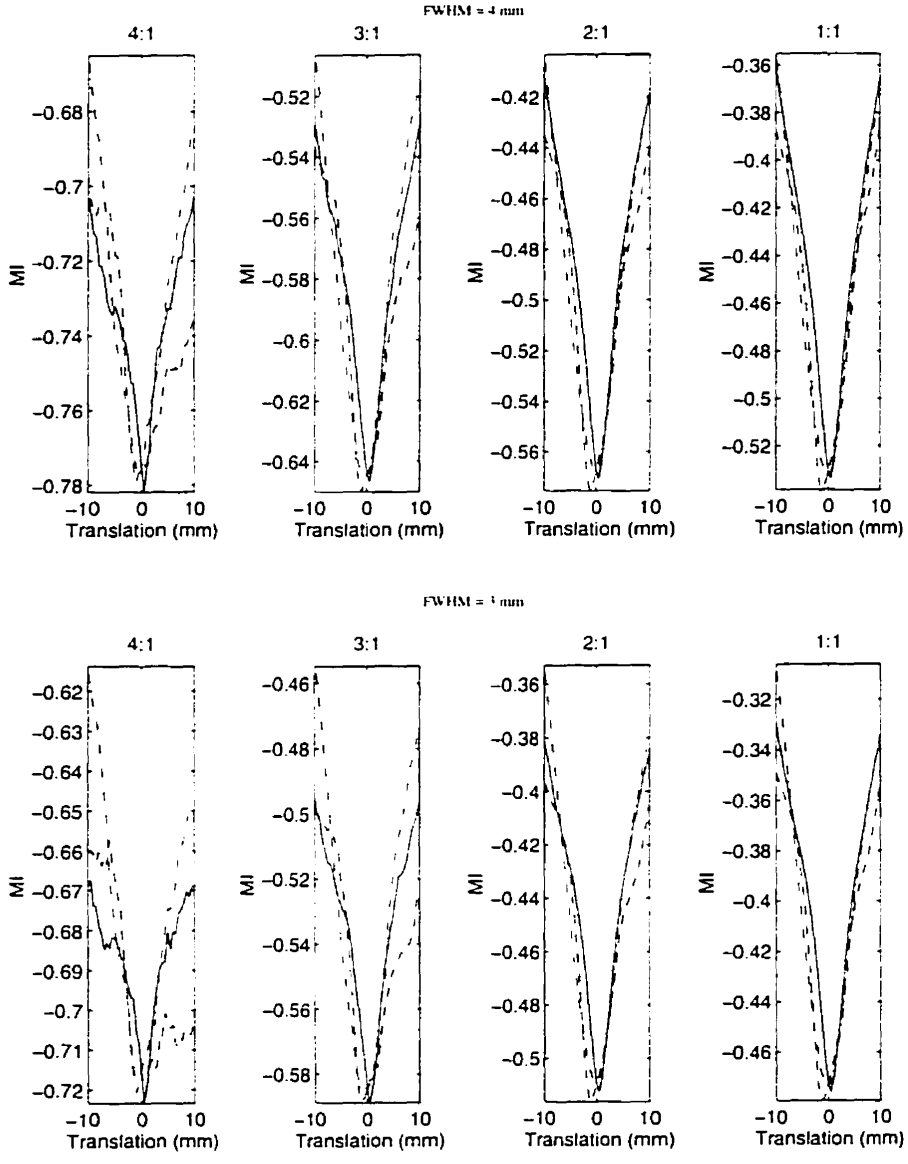

Figure 5.8: The effect of different sub-sampling rates on **MI** measurement. The MR data is blurred by 3-D Gaussian kernel with FWHM = 4 mm, 3 mm respectively before the **MI** versus translational misregistration calculation. The four columns from left to right correspond to sampling rates of $4:1, 3:1, 2:1$, and $1:1$ respectively. Solid line – along x direction, dashed line – along y direction, dash-dot – along z direction.

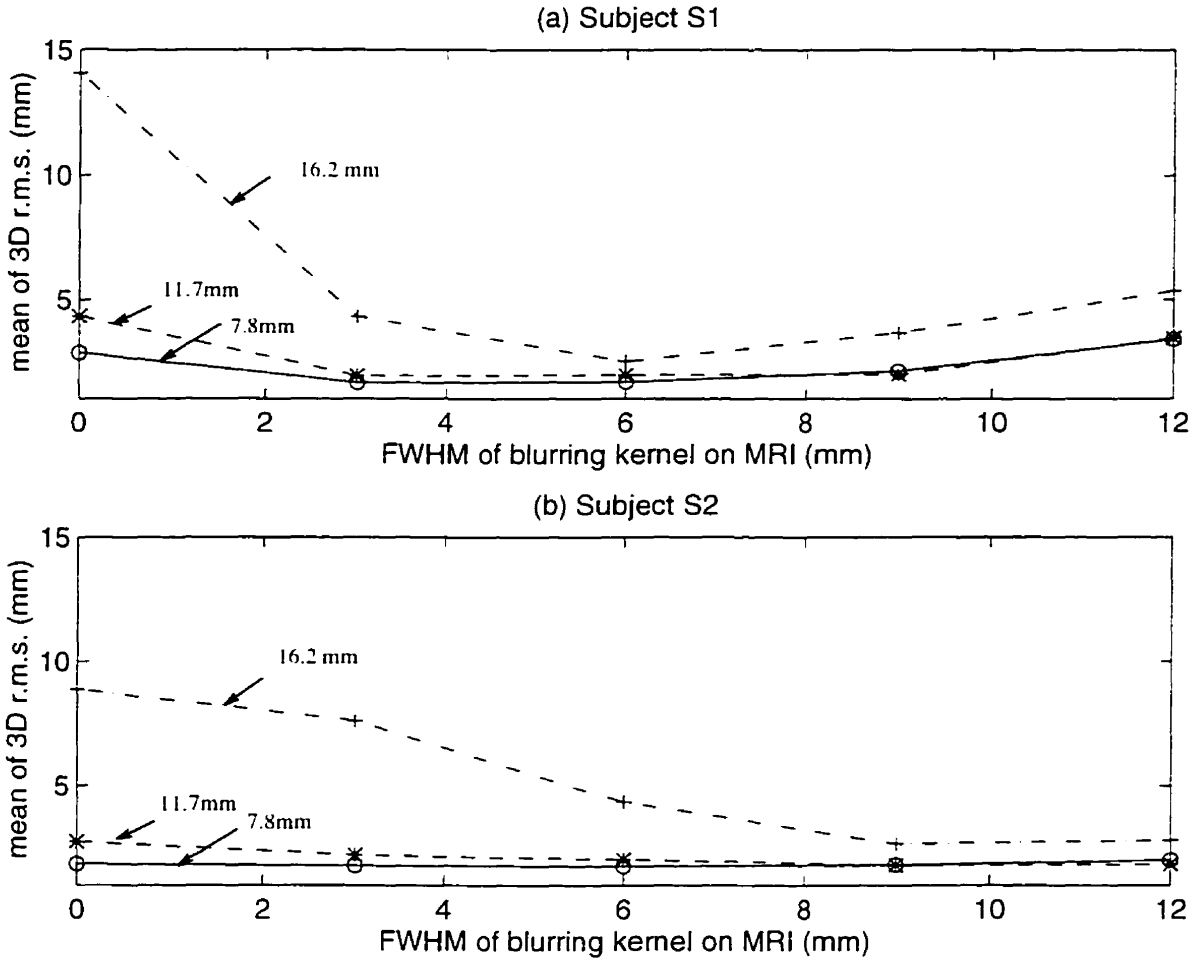

Figure 5.9: Registration errors from MRI and tPET images at various resolutions. The five MRI data sets are blurred by FWHM = 0 mm, 3 mm, 6 mm, 9 mm, and 12 mm respectively. The three curves represent tPET images at resolution of FWHM=7.8 mm, 11.7 mm, and 16.2 mm as indicated.

5.2.1.3 Interpolation Methods

The effect of interpolation methods on registration were also examined by analysis of the **MI** versus translational misregistration function curves. **MI** measurement with four different interpolation methods (nearest neighbor, trilinear, trilinear partial volume distribution, and tricubic) have been obtained from the same MRI and tPET data as above. The results shown in Figure 5.10 demonstrate that the nearest neighbor interpolation gives step-wise curves along each direction and the other three interpolation methods result in similar function curves.

5.2.2 Performance of Registration Methods

The performance of both **MI** and **VR** registration algorithms was assessed using different indices, including (1). registration accuracy, (2). stability against noise, (3). stability against spatial resolution of tPET image, and (4). robustness to data truncation. In Section 5.2.1, three implementation parameters including estimation of initial transformation method, sampling and blurring on MRI data and interpolation method were investigated on the **MI** method. These three parameters should have the same effect on both of the two voxel-based methods (**MI** and **VR**):

- The estimation method of initial transformation intends to get a better overlap of the two images at the beginning of the iteration, therefore the one which can give a larger overlap volume, will benefit any voxel-based registration method since the success of the voxel-based method depends on large number of voxels participating registration.

- A beter choice of sampling rate and blurring on MRI volume enables the two images from different modalities to have more matched information and quickens the registration procedure. Therefore, for the two voxel-based methods using the same matching features (i.e. voxel intensity) , the choice of these two parameters should only be affected by the data sets not by the method itself.

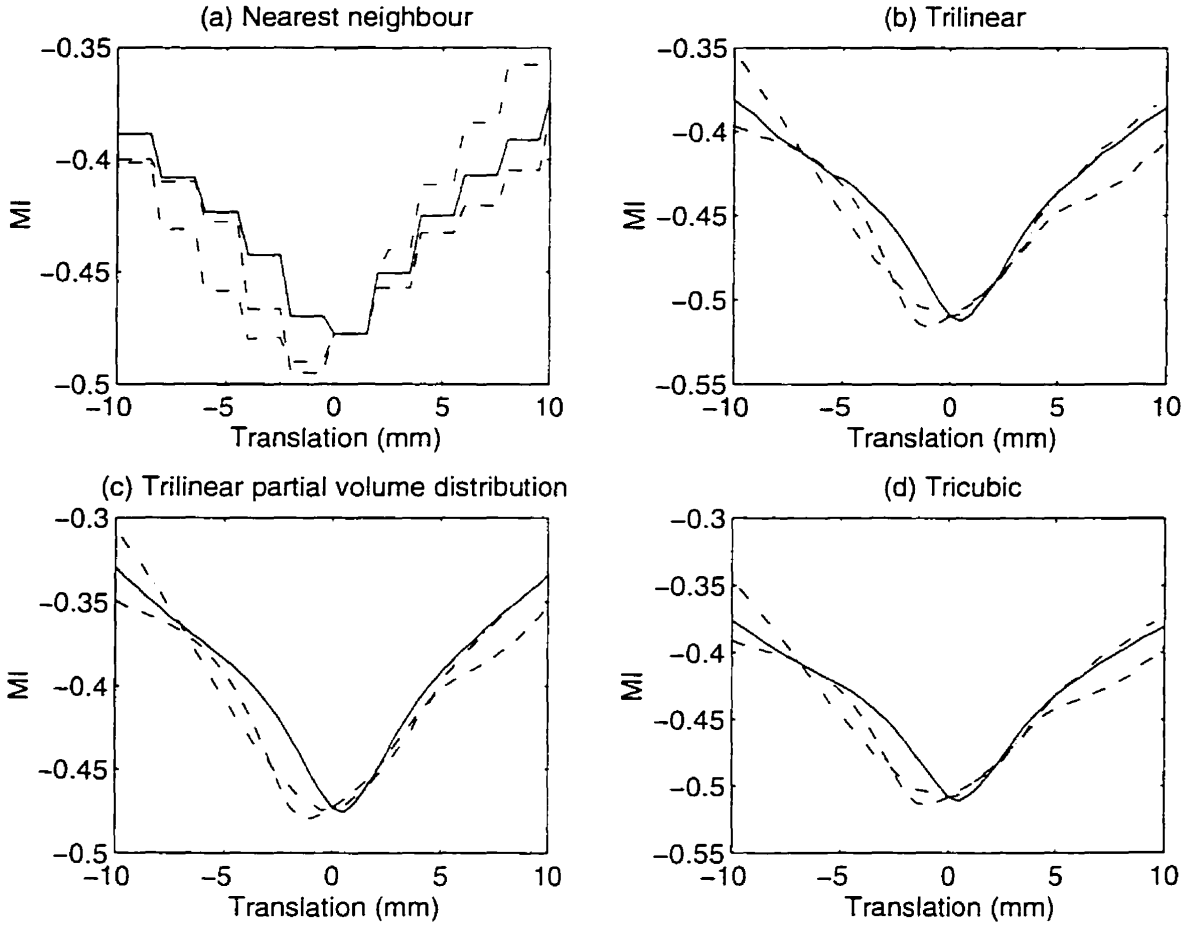

Figure 5.10: **MI** measurement versus translational misregistration under different interpolation methods.

MR data is blurred before calculation of **MI** measurement and sampled at rate of 1 : 1. Solid line - along x direction, dashed line - along y direction, dash-dot - along z direction.

(a) Nearest neighbor interpolation

(b) Trilinear interpolation

(c) Trilinear partial volume distribution interpolation

(d) Tricubic interpolation.

- The choice of interpolation method in this thesis is a trade-off accuracy and computation efficient. So we use the trilinear interpolation on both methods.

Based on these reasons, the same implementation parameters are used on both **MI** and **VR** methods.

5.2.2.1 Registration Accuracy

Experiment type A was applied to MRI and simulated tPET image I_{23} (FWHM = 11.7 mm and $N_{max} = 9M$) from both subject S1 and S2. Forty random transformations were applied on each subject. The 3-D misregistration errors of the results from the two registration algorithms are shown in Table 5.2.

The simulated tPET data image I_{23} is closest to the real ones obtaining during general clinical studies. The accuracy of the registration can be examined by the 3-D mean r.m.s. (Equation 4.7). The standard deviation of the r.m.s. values also indicates the stability of the registration algorithm. The **MI** method succeeded in all of the 80 runs on the two subjects (max r.m.s. < 2.5 mm), while 10% of the **VR** registrations have r.m.s. misregistration values of > 4 mm.

subject	method	mean r.m.s. (mm)	std r.m.s. (mm)	max r.m.s. (mm)
S1	MI	1.90	0.16	2.35
	VR	2.81	0.72	5.68
S2	MI	1.84	0.17	2.15
	VR	2.72	0.43	4.56

Table 5.2: 3-D misregistration errors on subject S1 and S2

5.2.2.2 Noise and Resolution

The performance of the registration algorithms against the noise and resolution of MR images was not investigated in this thesis. Compared with the tPET images,

MR images have much higher resolution and signal to noise ratio. Besides the intrinsic characteristics of the two image modalities, the MR images is blurred before registration in our implementation, therefore, the noise in MR images is negligible. The resolution and noise level of PET transmission images are the major effect on the MRI/tPET image registration.

The stability of the registration algorithms as a function of resolution and noise level in tPET images was examined using type A experiments (registration accuracy, see Section 5.1.1.2). The MR image was registered with each of the 12 simulated tPET images from the same subject. Twenty random transformations were used on each MRI/tPET image pair of both subjects of S1 and S2. Figure 5.6 demonstrates examples of the simulated tPET images. Figure 5.11 and 5.12 show the mean 3-D misregistration errors (Equation 4.7) for different total counts in the tPET image, using the **MI** and the **VR** methods respectively. In figure 5.12, the results from PET images at resolution of FWHM = 16.2 mm were not shown. The mean r.m.s. values from the registration results are all larger than 10 mm, which indicates that the **VR** method is very unstable for low resolution tPET images.

5.2.2.3 Data Truncation

MRI and PET scans on the same patient, when acquired at different times, might cover different parts of the brain. This partial overlap issue is a common problem in medical imaging.

To test the robustness of the method to truncation of MRI data, slices from MRI data were removed from bottom, top, or both from subject S2. Experiment type A was performed on the MRI data with missing data and the simulated tPET data. Twenty random transformations were applied on the MRI data in each trial.

Figure 5.13 gives the mean 3-D registration error of the registration as a function of the percentage of missing data from MRI data. It should be noted that the original MRI data cover larger (16%, vertical dash line mark in the figure) volume than tPET

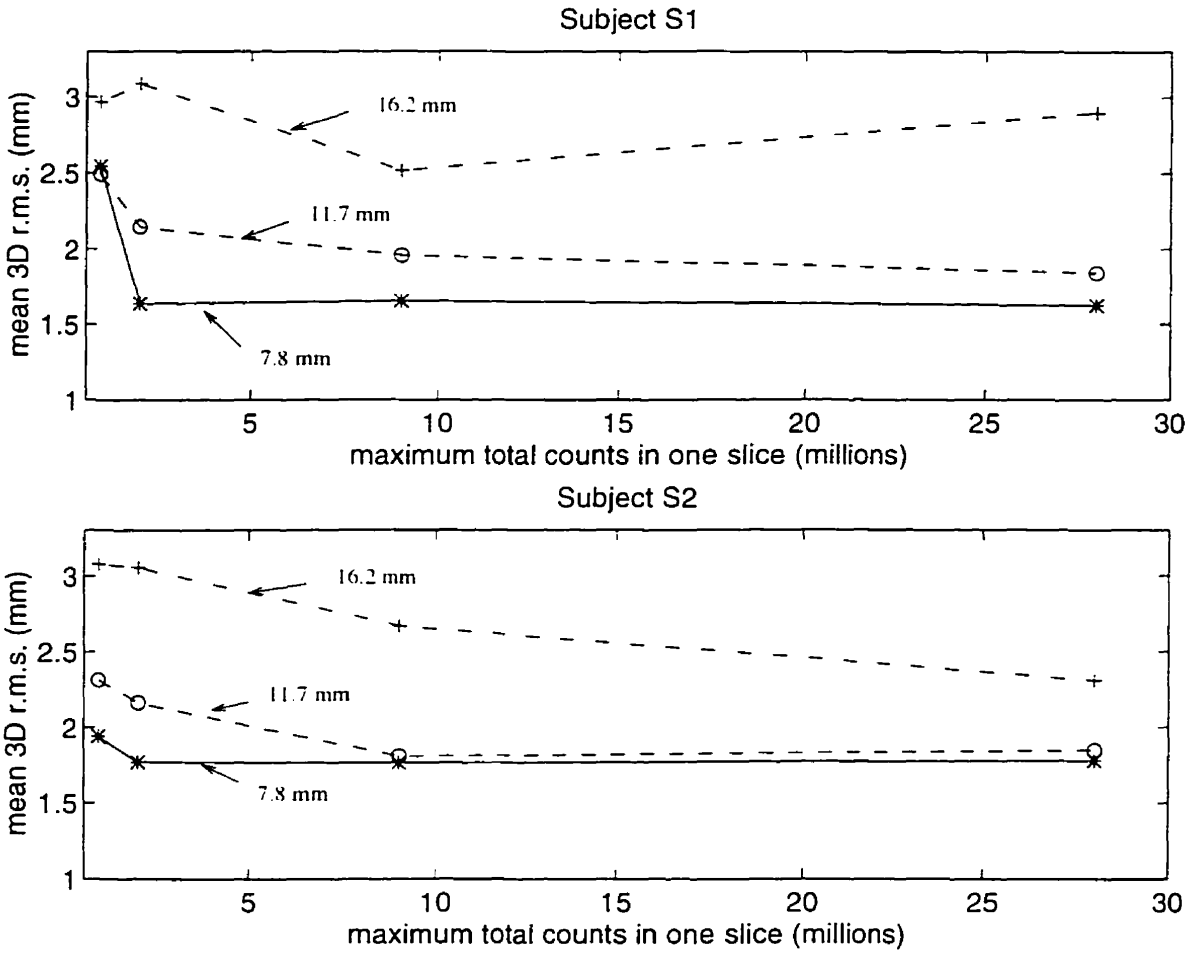

Figure 5.11: The dependence of the MI method upon resolution and noise in MRI/tPET registration. tPET images were blurred to 7.8mm, 11.7mm, and 16.2mm FWHM as shown.

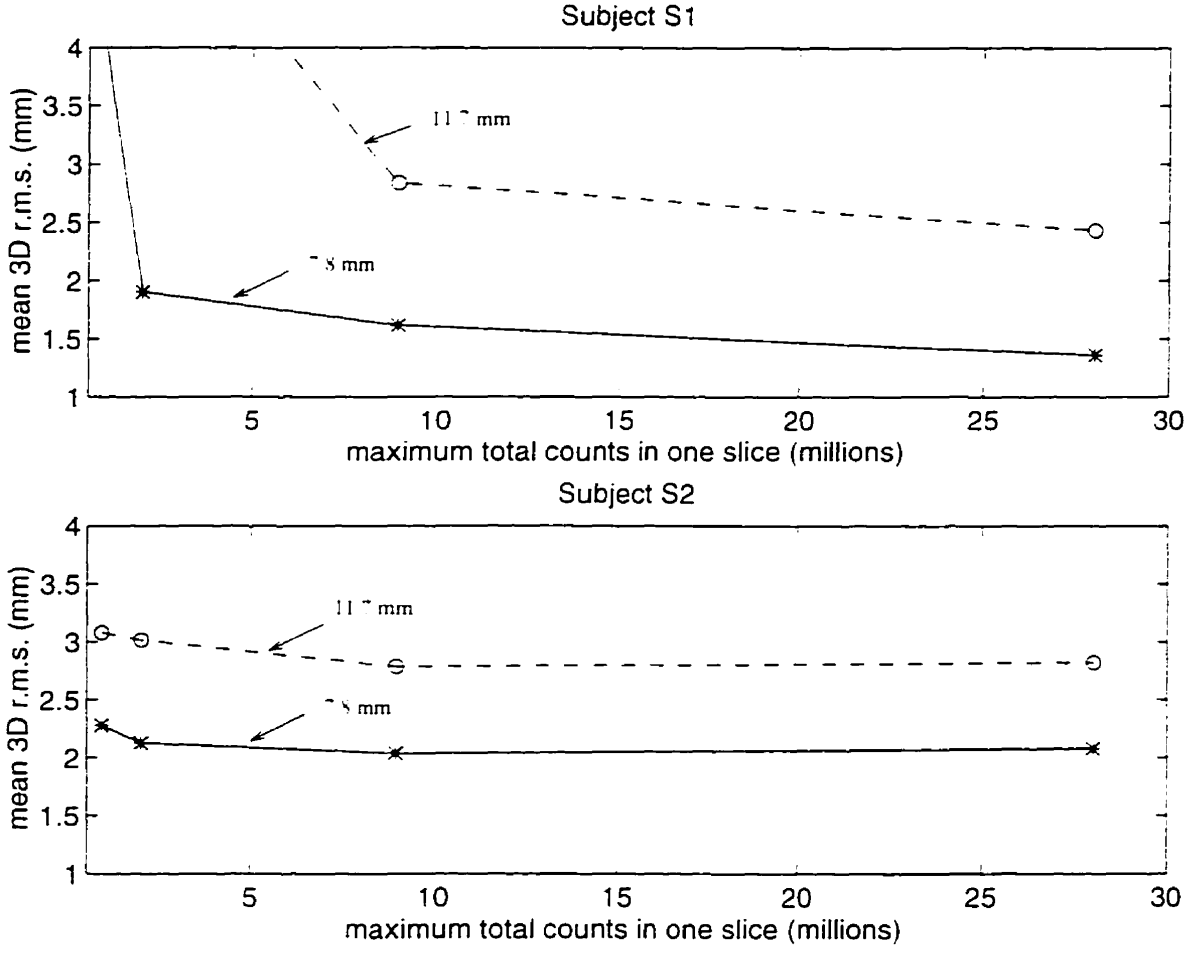

Figure 5.12: The dependence of the **VR** method upon resolution and noise in MRI/tPET registration. tPET images were blurred to 7.8mm, 11.7mm, and 16.2mm FWHM as shown.

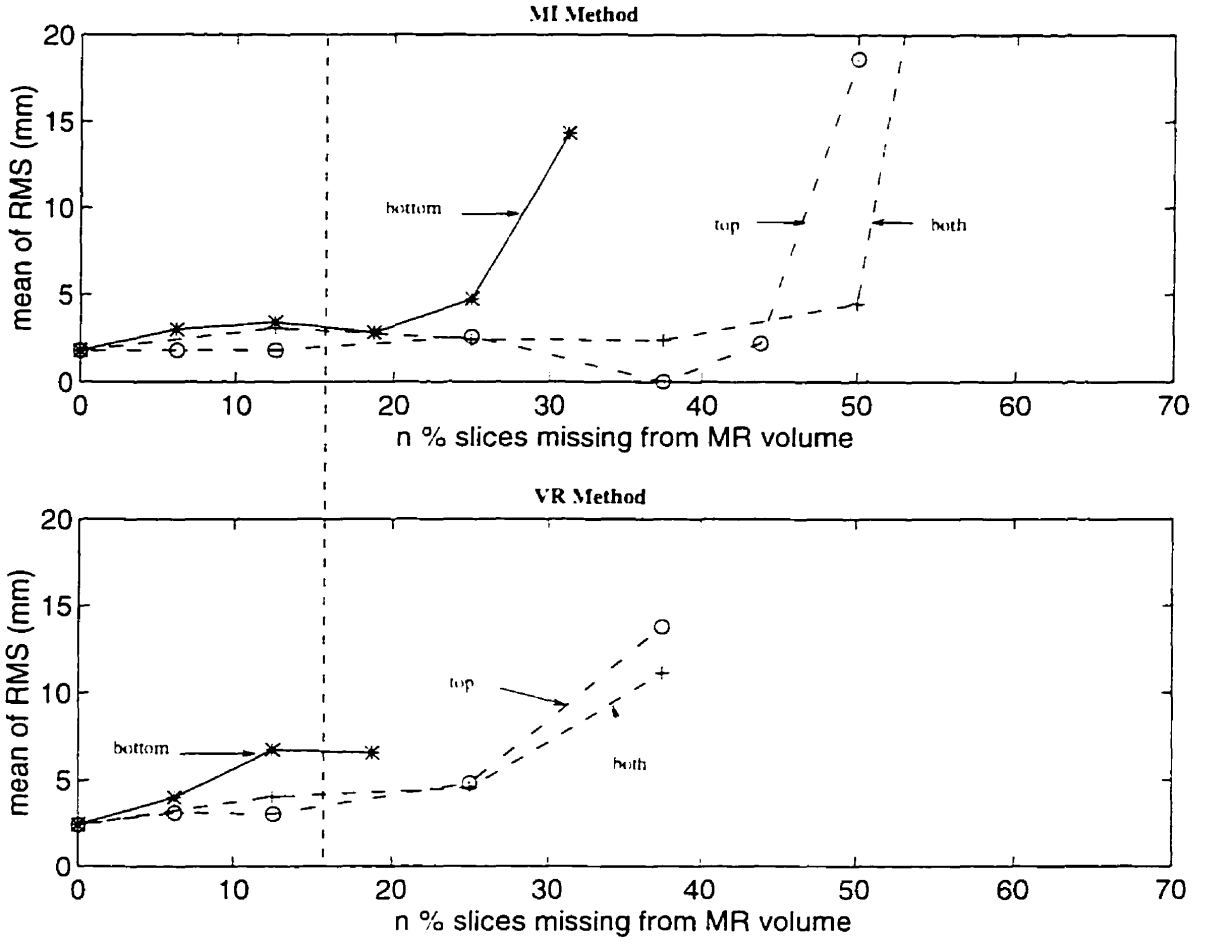

Figure 5.13: Robustness of **MI** and **VR** registration algorithms to data truncation of MR images. Solid line corresponds to slices removed from bottom, dash-dot line to slices from top and dashed line to slices from both top and bottom. The vertical dashed line corresponds the 16% MRI slices from top which have no corresponding structure in the tPET image.

data because the preprocessing step only cropped the MRI data to approximately cover the whole brain. Therefore, the first 16% data from top in MRI data have no corresponding part in tPET image, hence, this part might be removed without affecting the performance of registration algorithms. From the figure, it can be seen that the **MI** method is stable with up to 25% data missing from bottom, 28% (44% – 16%) from top and 34% (50% – 16%) from both. While the **VR** method can keep stable with 10% data missing from bottom, 9% (25% – 16%) from top, and 9% (25% – 16%) from both .

5.3 Results from the Experiments on Real Data Sets

Based on the experimental results from last section, we found that the **MI** method is more accurate and robust than the **VR** method. For real data sets, true registration results were unknown. Hence, an exact measure of misregistration was not possible. Therefore, it is not possible to quantitatively compare the registration accuracy between the two methods on the real data sets. For this reason, the experiments on the real data sets were only applied to the **MI** method to examine the performance of the method on the images from clinical studies.

The **MI** method was used to register 21 MRI/tPET image pairs (See section 5.1.2.1). Figure 5.14 shows two typical registered images. As can be seen from the right column, although part of the data was missing from the tPET image, the **MI** algorithm was still successful.

Visual inspection of the superimposed re-sampled MRI and tPET images from all 21 subjects demonstrated no obvious misregistrations.

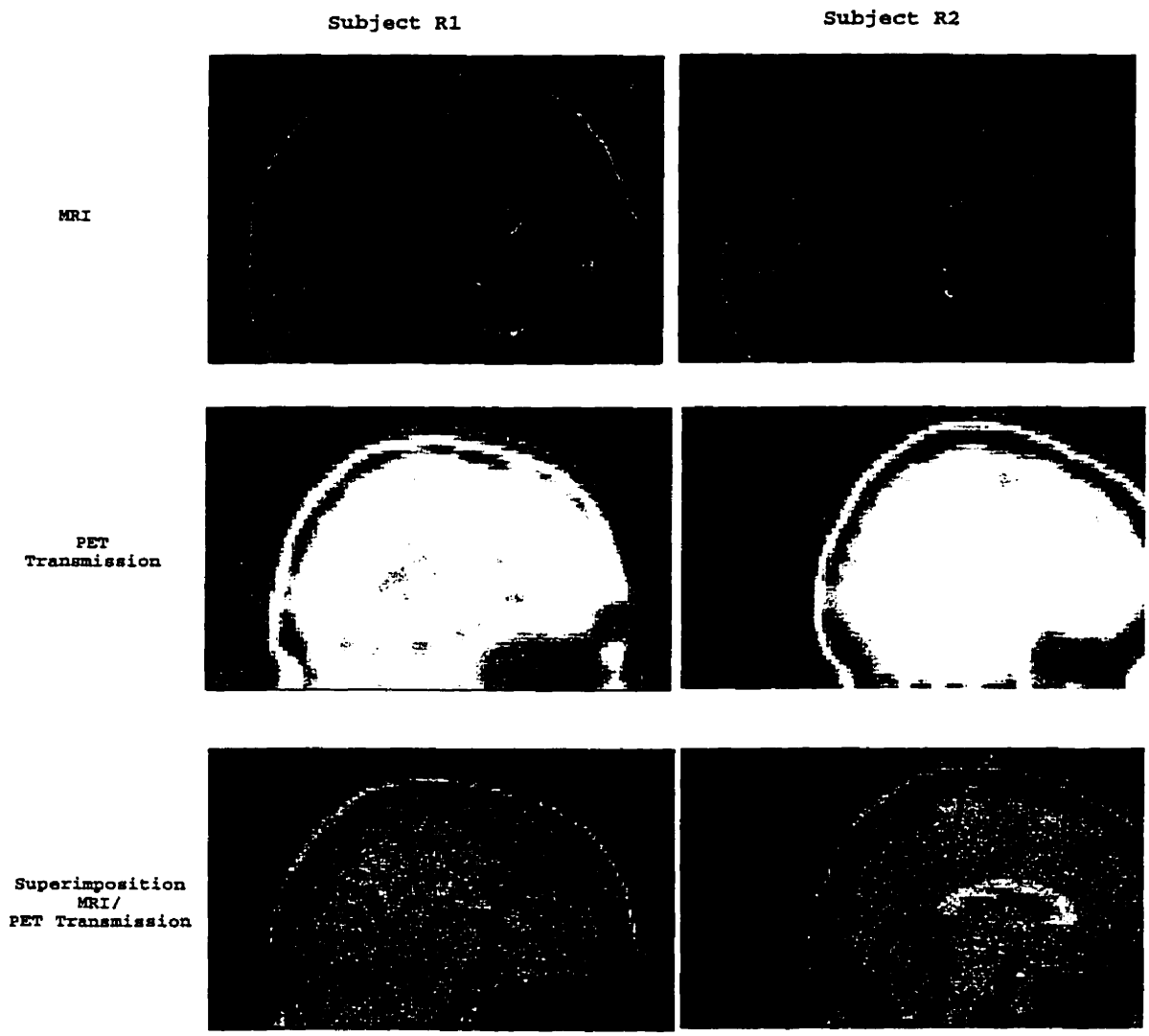

Figure 5.14: Registration on real data both tPET images were collected from Siemens ECAT HR+ scanner. The PET image on right column has part of data missing from the front of head.

5.4 Discussion

In this section, the first part discusses the issues related to the effect of implementation parameters on the **MI** method. The second part compares the performances between the **MI** and the **VR** methods.

5.4.1 Implementation Parameters

5.4.1.1 Volume Overlap at the Beginning of Registration

The experiments performed to evaluate two methods of estimation of the initial transformation indicate that the volume overlap at the beginning of registration is an important factor on the success of the **MI** algorithm. The random transformations in the experiment (Section 4.3.2) caused the two volumes to have small overlap if aligned by geometric center. The estimation of initial transformation by COG alignment has the advantage of providing better overlap of the two volumes. Since the use of a large number of voxels in a voxel-based registration is the principle reason for its robustness against noise contained in both images, larger overlap regions at the beginning of registration permit the **MI** algorithm to be more robust against random noise in both images. The similarity measurement can only indicate how well the two data sets match in the areas of overlap; therefore, at the initial position, if the MR and tPET images have significant non-overlap areas, the similarity measurement **MI** may be a local minimum and smaller than that obtained when the two volumes are correctly aligned.

The experiment (Section 5.2.1.1) also shows the by aligning COG, the initial estimation gives a better estimation on translation parameters, hence, the optimization converges more quickly (less iterations were performed).

5.4.1.2 Sampling and Blurring on MRI in the MI Method

The goal of blurring the MR image before registration was to reduce the effect of noise and subsampling, and to remove details visible at the highest resolution from the MR image, which no corresponding detail in the tPET image, may only introduce registration errors. The experiments on two simulated tPET images showed:

- A blurring kernel applied to MRI data before registration is necessary even with a fully-sampled MR image (See Section 5.2.1.2). This will let the two images have more corresponding information, i.e., decreasing the details from MR images, which have no correspondence in tPET images.

- For medium resolution PET data, e.g. FWHM = 7.8 mm and 11.7 mm, the MI method is not very sensitive to the width of the Gaussian kernel applied to the MRI data (See Figure 5.11 and Figure 5.12). A broad range of blurring kernel widths (FWHM from 3 mm to 9 mm) yielded similar good results at both PET resolutions. This is because that at this range of resolution, information from MRI and PET image have better match than those when MRI is not blurred or over-blurred.

- The FWHM of the blurring kernel should be bounded above by the resolution feature of interest, such as skull and scalp in MRI/ tPET registration. When the FWHM of blurring kernel is large enough to blur out these features, i.e. mixing scalp and skull in MRI data, the matching features between the images to be registered will be lost. Thus correct registration is hard to obtain in this case.

However, the two subjects gave different results when the tPET data were at resolution of FWHM = 16.2 mm and the MRI data were blurred with FWHM = 9 mm or 12 mm kernel, i.e. there is no explicit minimum in the r.m.s. error plot for subject S2.

Visual inspection of the two MRI data sets (Figure 5.2) shows that subject S1 has a thinner scalp than S2 and the contrast between scalp and skull in S1 is lower than that of S2. When S1 is blurred with a large FWHM kernel (i.e. FWHM = 9 mm), the scalp and skull cannot be distinguished from each other clearly. On the other hand, the tPET data has high contrast between the scalp and skull tissue. When blurred with the same kernel, the intensity difference between scalp and skull is still quite clear for subject S2. Therefore, there is a trade-off between retaining the feature of interest (e.g. skull and scalp) and removing details and noise from the MRI data. The results suggest that a filter FWHM of 6 mm be chosen as a compromise for practical use.

5.4.1.3 Interpolation Methods in MI Method

From the four **MI** measurement, as a function of translational misregistration plots obtained by using different interpolation methods (Figure 5.10), the nearest neighbor interpolation, which is the fastest interpolation among the four methods, gives a step-wise curve due to the large voxel size of tPET data. From the flat response around the true registration position, it is apparent that the nearest neighbor interpolation can not give results with sub-voxel accuracy.

For the other three interpolation methods, the trilinear and trilinear partial volume distribution interpolation methods give quite similar results. Although the initial intent to use trilinear partial volume distribution interpolation instead of trilinear interpolation was to avoid unpredictable changes in the histogram of the target volume, the trilinear interpolation shows no sign of ill-behavior from the **MI** versus translational misregistration function (Figure 5.10). Due to the low resolution and large interval between slices along the z direction of transmission data, the more sophisticated tricubic interpolation does not gain much advantage over the trilinear methods.

Therefore, due to the fast speed of the trilinear interpolation method (approximately six times faster than the tricubic interpolation), it was used throughout the

experiments in this thesis.

5.4.1.4 Noise and Resolution Effect in MI Method

The experiments on the stability of the **MI** algorithm to resolution and noise level of the tPET data (Figure 5.11) show that the two curves representing resolutions of FWHM = 11.7 mm and 7.8 mm are very close when $N_{max} \geq 9M$. When the resolution is high (FWHM= 7.8 mm), the registration error is still below 2 mm even for tPET data having low counts, i.e. $N_{max} = 2M$. These results suggest that the algorithm is less sensitive to noise than it is to spatial resolution. Since the **MI** algorithm uses a large number of voxels in the similarity calculation and the noise in the data sets is randomly distributed, the algorithm is robust to noise. However, low spatial resolution (i.e. FWHM $\geq$ 16.2 mm) of the tPET image may cause a shift of the features of interest, affecting the registration accuracy. In Figure 5.11, the results from subject S1 shows that the mean registration error at $N_{max} = 28M$ is larger than that at $N_{max} = 9M$ for FWHM = 16.2mm , due to one large r.m.s. value in the trial. This demonstrates that the spatial resolution affects the **MI** algorithm more than does noise, and the algorithm is less stable when the tPET image is at low spatial resolution.

5.4.2 Comparison Between MI and VR Methods

The second set of experiments of MRI/simulated tPET image registration were performed on both the **MI** and the **VR** methods. The registration accuracy experiments (Section 5.2.2.1) show a mean accuracy from **MI** method was of < 2 mm while it was larger than 2.7 mm from **VR**. This indicates that the **MI** method can give more accurate registration results than the **VR** method from the clinical-like simulated PET images. The standard deviation value of the r.m.s. (Table 5.2) shows that the **MI** method (std r.m.s. < 0.2 mm) is more stable than **VR** method (std r.m.s. > 0.4 mm).

The experiments on the robustness of the methods against noise and spatial resolution (Section 5.2.2.2) show that both the **MI** and the **VR** methods are more sensitive to spatial resolution than to noise. However, the **VR** method deteriorated much faster than the **MI** method when decreasing the spatial resolution of the PET image (i.e. for the **VR** method, mean 3-D registration error r.m.s. $>$ 10 mm when the FWHM of PET image is 16.2mm).

Data truncation experiments (Section 5.2.2.3) demonstrate that the **MI** method is more robust to the data truncation from MR images than the **VR** method. With up to 25% slices missing from MR image, the **MI** method could still work well. But the **VR** method could not remain stable when more than 10% slices missing from MR images.

From the experiments in Section 5.2.2, we conclude that the **MI** method is more suitable for the MRI/tPET image registration problem. The **MI** method can achieve sub-voxel accuracy ($<$ 2 mm) for practical clinical studies. It is more stable than the **VR** method when the PET image has low spatial resolution and high noise levels. The **MI** method is also more robust to the partial overlap issue than the **VR** method.

In the **VR** method, the similarity measurement is most effective if the intensity partitions can be best matched to the true tissue classification (i.e. the same intensity values represent similar tissue types). However, in T1-weighted MR images, the intensity values of scalp and white matter are close to each other, therefore in MRI/ePET image registration, the non-brain structures have to be removed before registration. In MRI/tPET image registration, the scalp and skull both contain very important information to match PET image with MR images. Thus, the scalp and skull should not be removed from the MR image. On the other hand, keeping the scalp may cause the variance of intensity ratio similarity measurement to be less effective, and thereby causing the **VR** method to be less accurate and robust than the **MI** method.

Another possible reason for the **MI** method being more accurate and robust than the **VR** method is that the **MI** method measures the feature space histogram from

both dimensions while the variance of intensity ratio measurement works in one dimension, i.e. it is asymmetric. Since the **VR** measurement is calculated along one axis (i.e. the MRI axis in MRI/PET registration) of the feature space histogram, it can only assign large variance value to the MRI partitions (voxels with same MRI intensity value in the **VR** method) where the intensities in the corresponding PET regions are not uniform. On the other hand, when the uniform regions in the PET image corresponds to non-uniform regions in the MR image, the **VR** method will not directly make the variance value higher since the MR image is taken as the denominator image in the **VR** measurement. The **MI** method calculates the similarity measurement on the feature space histogram symmetrically. Therefore, both cases described above increase the similarity measurement (**MI**) value instead of only one case does in the **VR** method, where uniform region in denominator image corresponds to non-uniform region in numerator image.

Chapter 6

Conclusion and Future Related Work

In this chapter, future research work related to the tracer-independent MRI/PET registration problem is discussed first, followed by the final conclusion of this thesis.

6.1 Future Related Work

Two directions of research work can be carried out:

- More evaluation experiments should be performed on both simulated and real data sets to get a better understanding of the effect of various implementation parameters on the registration algorithm.
- Improve the tracer-independent MRI/PET registration method with respect to registration accuracy.

6.1.1 More Evaluation Experiments on the Registration Algorithm

6.1.1.1 Experiment on Simulated PET Transmission Images

The experiments in Chapter 5 show that the filter width of the blurring kernel should be limited by the resolution of the features of interest (i.e. skull and scalp in PET images). More experiments on MRI/PET data sets from different subjects should be performed to prove this and give a more strict criterion and an adaptable method for choosing the filter width of the blurring kernel automatically for each subject.

Various experiments have shown that the **MI** method is more sensitive to spatial resolution than to the noise of PET transmission image. With PET images at higher spatial resolution, the algorithm should give more accurate registration results. The Siemens ECAT HR+ scanner at the MNI can provides tPET images at higher resolutions and with larger FOV than the older Scanditronix PC-2048 scanner. Simulated tPET images generated based on the geometry of this new scanner should be used to prove this conclusion. From these quantitative evaluation results, the method can be widely used in the research work based on the PET images from the Siemens scanner.

6.1.1.2 Quantitative Evaluation of the MI Algorithm on Real PET Transmission Images

The validation experiments on real MRI and tPET images described in Chapter 5 were not quantitative. The exact registration accuracy could not be evaluated by the visual inspection. Therefore, the quantitative assessment on the registration accuracy of the algorithm on real data sets is desirable. The registration result from extrinsic landmark-based registration algorithm can be used as the reference to measure the registration error [19, 63]. On the other hand, registration results from other registration methods (i.e. surface-based method and intrinsic landmark-based method) on the same data sets can be used to evaluate the consistency of the **MI** registration

algorithm.

Another experiment will be very interesting to furtherly verify the **MI** and **VR** methods, in which the registration methods are to register real MR image to both real and simulated tPET images of the same patient. Comparing the two registration results will help the validation of both simulated PET technology described in Section 5.1.1.1 of this thesis and the registration method itself.

6.1.2 Incorporating More Matching Features to Improve the Registration

In our voxel-based MRI/tPET image registration algorithms, only voxel intensity is taken as the matching feature. The advantage of using this matching feature is its simplicity and robustness, because no feature extraction procedure is required. Collins et al. [61] demonstrated that using two matching features (i.e. voxel intensity and gradient magnitude) allows the registration algorithm to be more robust than using only one matching feature. Although not all gradient information from the original MRI and PET image are equivalent (i.e. the tissues within the skull are almost uniform in tPET image), it is possible to get some equivalent gradient information from the blurred MR image, in which the fine details in brain are removed. For example, both MRI and tPET image have large intensity changes around the scalp and skull area, which can yield strong gradient magnitude values. These strong gradients will have a positive effect on the registration accuracy.

However, incorporating gradient information into existing voxel-intensity-based registration method must consider the following two issues in order to make the registration more accurate and robust:

- How to remove the fine details from MRI data while keeping the contrast between skull and scalp strong, and the gradient information in these regions not shifted. In this case, the choice of filter width of the blurring kernel may be more

critical to the success of the registration than that in the intensity matching.

- The effect of gradient matching on the whole registration procedure. There are two possible ways to incorporate the gradient matching into the whole registration procedure. Firstly, the gradient matching can be taken only as a fine tuning approach. For example, we can limit the range of changes on the transformation parameters of the registration result obtained from voxel-intensity-based matching. Secondly, we can have the gradient matching affect the transformation parameters as equally as the intensity-based matching. Gradient operation might give spurious information due to noise and gradient matching may be not as robust as the intensity-based matching against noise though both methods use large number of voxels. Therefore, a preliminary analysis on the robustness of the gradient matching against noise in the images should be performed first. If the analysis shows the gradient matching is not as robust as the intensity-matching, the first method (using gradient matching as a fine-tune approach) may still be used.

Besides the matching feature, the optimization procedure used in this thesis (Powell algorithm) may be improved. For example, compared with the Newton-Raphson algorithm, the Powell algorithm calculating much more times of similarity measurements, which is very computation-intensive due to large number of voxels participating the computation. Although the true derivative value of mutual information can not be obtained, numerical approximation may be adequate to make the derivative-based algorithm work in the MI method which will greatly improve the efficiency of the optimization procedure.

6.2 Conclusion

This thesis describes an automated tracer-independent MRI/PET registration method, which is based on the spatial aligned relationship between the tPET and ePET images.

In this method, the registration of the MR image with the ePET image is accomplished automatically by the registration of the MR image with the corresponding tPET image. Because tPET images carry the same anatomical information regardless of the tracer used in the PET studies, the registration of MRI/PET transmission images allows the MRI/PET registration performed in a tracer-independent fashion. This tracer-independent registration method is especially useful in two cases:

- The tracers used in some PET studies accumulate in a small region. The PET emission images in these studies do not provide enough anatomical information to match with MR images.

- Even with the tracer that accumulates throughout the entire brain, the PET images from the patients with tumor or stoke may contain large regions of abnormal accumulations.

Two voxel-based registration methods were implemented to register MR and tPET images in this thesis. The mutual information method (**MI**), which is based on information theory, uses the mutual information of corresponding intensity values from the two images to measure how well the two images match to each other. The variance intensity ratio method (**VR** tries to minimize the variance of intensity ratio throughout the volumes to register the two images. These two voxel-based methods, compared with point-landmark-based methods and surface-based methods, do not require feature extraction procedure before the registration and use large number of voxels in the registration. Therefore, these two methods are more robust to the noise and partial overlap of the two image volumes.

The validation of the registration methods was performed on both simulated and real tPET images with real MR images. The quantitative evaluation of the two methods on simulated PET transmission images with MR images indicates:

1. The **MI** method gives more accurate registration result than the **VR** method in MRI/tPET image registration. With PET images at resolution $\leq$ 12 mm

and $N_{max} \geq 9$ M, the **MI** method gives 3-D mean registration error less than 2 mm.

2. The **MI** method is more stable than the **VR** method when the PET transmission image has a high noise level. With tPET image having total counts $N_{max} < 1M$, the **MI** method shows registration error < 3.5mm for both S1 and S2 subjects and the **VR** method shows error > $5mm$ for S1. (See Figure 5.11 and 5.12).

3. Both methods are more sensitive to spatial resolution than the noise in PET transmission image. The **VR** method seems to deteriorate more quickly than the **MI** method with the spatial resolution of PET transmission image decreasing.

4. The **MI** method is more robust than the **VR** method in the case of data truncation in MR images.

5. The blurring procedure before subsampling MRI data in the registration allows the multi-resolution optimization to be more robust against noise in the images and more efficient.

MRI/PET image registration is a valuable technique to facilitate the investigation of brain function, the clinical diagnosis and treatment. The tracer-independent registration algorithm developed in this thesis greatly increases the possibility of accurate registration of MRI to ePET images in any tracer studies. Further improvement and validation of this algorithm will enhance the employment of this method in both research and clinical environment.

Reference

[1] Evans AC. Beil C. Thompson CJ. Hakim A. *Anatomical-Functional Correlation Using an Adjustable MRI-Based Region of Interest Atlas with Positron Emission Tomography.* Journal of Cerebral Blood Flow and Metabolism. 8:513-530. 1988.

[2] Evans AC. Marrett S. Collins L. Peters TM. *Anatomical-funcational correlative analysis of the human brain using thre-dimensional imaging systems.* Proc. SPIE 1092:264-274. 1989.

[3] Valentino DJ. Mazziotta JC. Huang HK. *Mapping brain function to brain anatomy.* Proc. SPIE 194:445-451. 1988.

[4] Pelizzari CA.Chen GTY.Spelbring DR. Weichselbaum RR. Chen CT. *Accurate Three-Dimensional Registration of CT. PET. and/or MR Images* Journal of Computer Assisted Tomography 13(1):20-26. Jan/Feb. 1988.

[5] Evans AC. Marrett S. Torrescorzo J. Ku S. Collins L. *MRI-PET Correlation in Three Dimensions Using a Volume-of Interest (VOI) Atlas.* Journal of Cerebral Bolld Flow and Metabolism. 11:A69-78. 1991.

[6] Raichle ME. *Positron emission tomography.* Annual Review of Neuroscience 1983; 6:249-267.

[7] Yamamoto YL. Thompson CJ. Diksic M. Meyer E. Feindel WH. *Positron emission tomography.* Neurosurgical Review 1984: 7(4):233-252.

[8] Phelps ME. Mazziotta JC. Huang SC. *Study of cerebral function with positron computed tomography.* J. of Cerebral Blood Flow & Metabolism. 1982; 2(2):113-162.

[9] Miura S. Kanno I. Iida H. Murakami M. Takahashi K. Sasaki H. Inugami A. Shishido F. Ogawa T. Uemura K. *Anatomical adjustments in brain positron emission tomography using CT images.* Journal Computer Assisted Tomography 12:363-367. 1988.

[10] Meltzer CC. Bryan RN. Holcomb HH. Kimball AW. Mayberg HS. Sadzot B. Leal JP. Wagner HN Jr. Frost JJ. *Anatoimcal localization for PET using MR imaging.* Journal of Computer Assisted Tomography 14:418-426. 1990.

[11] Brown GL. *A Survey of Image Registration Techniques.* ACM Computing Surverys. Vol. 24. No 4. December 1992. pp. 325-376.

[12] Venot A. Liehn J-C. Lebruchec J-F. Roucayrol J-C. *Automated comparison of scintigraphic images.* J. Nucl Med. 27:1337-1342. 1986.

[13] Mintun MA. Lee KS. *Mathematical realignment of paired PET images to enable pixel-by-pixel subtraction.* J. Nucl Med. 31:816. 1990.

[14] Minoshima S. Berger KL. Lee KS. Mintun MA. *An automated method for rotational correction and centering of three-dimensional functional brain images.* J Nucl Med. 33:1579-1585. 1992.

[15] Woods RP. Cherry SR. Mazziotta JC. *A rapid automated algorithm for accurately aligning and reslicing PET images.* Journal of Computer Assisted Tomography 16:620-633 1992.

[16] Evans AC. Collins DL. Mills SR. Brown ED. Kelly RL. Peters TM. *3D statistical neuroanatomical models from 305 MRI volumes.* IEEE Nuclear Science Symposium & Medical Imaging Conference, 1994. p 1813-1817.

[17] Collins DL. Holmes CJ. Peters TM. Evans AC. *Automatic 3D model-based neuroanatomical segmentation.* Human Brain Mapping 3: 190-208 (1995)

[18] Steinmetz H. Seitz RJ. *Functional anatomy of language processing: neuroimaging and the problem of individual variability.* Neuropsychologia. 1991: 29:1149-61.

[19] Alpert NM. Bradshaw JF. Kennedy D. Correia JA. *The principal axis transformation - a method for image registration.* J Nucl Med 31:1717-1722. 1990.

[20] Collier JM. Petti PL. Daftari I. Whitcomb T. Pitluck S. Kessler ML. *The Clinical Use of Image Correlation (MRI to CT) for Tumors of the Head in Charged Particle Radiotherapy.* Med. Phys. 17.552(A). 1990.

[21] Phillips MH. Kessler ML. Chuang F. Frankel KA. Lyman JT. Fabrikant JI. Levy RP. *Image Correlation of MR and CT in Treatment Planning of Intracranial Vascular Malformations.* Int. J. Radiat. Oncol. Biol. Phys. 20. 881-889. 1991 of the Brain. Journal of Computer Assisted Tomography. 13(1):20-26. 1989.

[22] Hill. DLG et. al. *Accurate Frameless Registrationof MR and CT Images of the Head: Applications in Surgery and Radiotherapy Planning.* Radiology 191:447-454. 1994.

[23] Evans AC. *Correlative Imaging.* In Principles of Nuclear Medicine. Wagner H. Zsabo Z. Buchanan J (Eds) pp. 405-421. 1995.

[24] Carson RE. Daube-Witherspoon ME and Green MV. *A Method for Postinjection PET Transmission Measurements with a Rotating Source.* J. Nucl Med 29:1558-1567. 1988.

[25] Thompson CJ. Ranger NT. Evans AC. *Simultaneous Transmission and Emission Scans in Positron Emission Tomography.* IEEE Transactions on Nuclear Science. Vol 36. No 1. February 1989.

[26] Thompson CJ, Ranger NT, Evans AC, Gjedde A. *Validation of Simultaneous PET Emission and Transmission Scans.* J Nucl Med 32:154-160, 1991.

[27] Hoffman EJ, Phelps ME. *Positron Emission Tomography: Principles and Quantitation.* In Positron Emission Tomography and Autoradiography: Principles and Applications for the Brain and Heart, eds M.E. Phelps, J.C. Mazziotta, H.R. Schelbert. Raven Press 1986 pp. 237-286.

[28] Eriksson L,Dahlbom M, Widen L. *Positron emission tomography - a new technique for studies of the central nevous system.* Journal of Microscopy. 157 : 305-333, Mar. 1990.

[29] Brooks RA and DiChiro G. *Principles of CAT in radiographic and radioisotope imaging.* Phys. Med. Biol. 21, pp. 689-732, 1976.

[30] Herman GT. **Image Reconstruction from Projections - The Fundamentals of Computerized Tomography.** Academic Press, New York, 1980.

[31] van den Elsen, PA, Pol, EJD, Viergver M.A.. *Medical Image Matching - A Review with Classfication.* IEEE Eng. Med. Biol. 12, pp26-39, 1993.

[32] Maurer CR, Fitzpatrick JM. *A Review of Medical Image Registration.* In Maciunas RJ (eds) Interactive Image-Guided Neurosurgery. pp 17-44, American Association of Neurological Surgeons, 1993.

[33] Wilson MW, Mountz JM. *A reference system for neuroanatomical localization on functional reconstructed cerebral images.* J Comput Assist Tomogr 13:174-178, 1989.

[34] van den Elsen P, Viergever MA. *Marker-guided registration of electromagnetic dipole data with tomographic images.* In Colchester ACF, Hawkes DJ (eds): Lecture Notes in Computer Science 511: Information Processing in Medical Imaging. Heidelberg: Springer-Verlag, pp. 142-153, 1991.

[35] van den Elsen P. Viergever MA. Van huffelen AC. Van der Meij W. Wieneke GH. *Accurate matching of electromagnetic dipole data with CT and MR images.* Brain Topogr 3:425-432. 1991.

[36] West J. Fitzpatrick JM. Dawant BM et. al. *Comparison and evaluation of retrospective intermodality image registration techniques.* Proc SPIE Medical Imaging. Vol 2710. pp. 332-347. 1996.

[37] Bergstrom M. Boethius I. Eriksson L. Greitz T. Ribbe T. Widen L. *Head fixation for reproducible position alignment in transmission CT and positron emission tomography.* Comput. Assist. Tomogr. 5. 136-141. 1981.

[38] Peters TM. Clark JA. Olivier A. Marchand EP. Mawko G. Dleumegarde M. Muresan M. Ethier R. *Integrated stereotaxic imageing with CT. MR imaging and digital subtraction angiography.* Radiology 161.821-826. 1986.

[39] Kall B. Kelly PJ. Goerss S. *Comprehensive computer-assisted data collection. treatment planning and iteractive surgery.* Proc SPIE 767:509-514. 1987.

[40] Kelly PJ. Kall B. Goerss S. *Functional stereotactic surgery utilizing CT data and computer generated stereotactic atlas.* Acta Neurochir Suppl (Wien) 33:577-583. 1984.

[41] Olivier A. Bertrand G. Peters TM *Stereotaxic systems and procedures for depth electrode placement: Technical aspects.* Appl Neurophysiol 46:37-40. 1983.

[42] Peters TM. Clark JA. Pike GB. Henri C. Collins L. Leksell D. Jeppsson O. *Stereotactic neurosurgery planning on a personal-computer-based workstation.* J Digit Imaging. 2:75-81. 1989.

[43] Zhang J. Levesque MF.Wilson CL. Harper RM. Engel J. Lufkin R. Behnke EJ. *Multimodality imaging of brain structures for stereotactic surgery.* Radiology. 175. 435-441. 1990.

[44] Bookstein F. *Thin-plate splines and the atlas problem for biomedical images.* In Colchester ACF. Hawkes DJ (eds): Lecture Notes in Computer Science 511: Information Processing in Medical Imaging. Heidelberg: Springer-Verlag. pp. 326-343. 1991.

[45] Mizziotta JC. Valentino D. Grafton S. Bookstein F. Pelizzari C. Chen GTY. Toga AW. *Relating structure to function in vivo with tomographic imaging.* In: Derek J. Chadwick JW (eds): Exploring Brain Functional Anatomy with positron Emission Tomography. Ciba Foundation Symposium No. 163. New York: John Wiley & Sons. pp. 93-112. 1991.

[46] Mizziotta JC. Pelizzari CA. Chen GY. Bookstein FL. Valentino D. *Region of interest issues: The relationship between structure and function.* J Cereb Blood Flow metab 11:A51-A56. 1991.

[47] Schonemann P. *A generalized solution of the orthogonal Procrustes problem.* Psychometrika 31:1-10. 1966.

[48] Sibson R. *Studies in the robustness of multidimensional scaling: Procrusted statistics.* J. Statist Soc B 40:234-238. 1978.

[49] Marrett S. Evans AC. Collins DL.Peters TM. *A Volume of Interest (VOI) atlas for analysis of neurophysiological image data.* In: Schneider RH. Swyer III SJ. Gibert Jost R (Eds) : Proc SPIE vol 1092. Med Im III: Image Processing. SPIE Press. Bellingham. pp 467-477. 1989.

[50] Goldstein H. **Classical Mechanics** Reading. MA: Addison Wesley. 1959.

[51] Hill DLG. Hawker DJ.Crossman JE. Gleeson MJ. Cox TCS. et al. *Registration of MR and CT images for Skull base surgery using point-like anatomical features.* Britian Journal of Radiology 64(767):1030-1035.1991.

[52] Levin DN. Pelizzari CA. Chen GTY. Chen CT. Copper MD. *Retrospctive geometric correlation of MR. CT and PET images.* Radiology 169: 817-823 1988.

[53] Levin DN. Hu X. Tan KK. Galhotra S. Pelizzari CA. Chen GTY. Beck RN. Chen C-T. Cooper MD. Mullan JF. Hekmatpanah J. Spire J-P. *The brain: Integrated three-dimensional display of MR and PET images.* Radiology 172:783-789.

[54] Niew HM. Chen C-T. Lin Wc. Pelizzari CA. *Automated three-dimensional registration of medical images.* Proc SPIE Med Imag III 1445:259-264. 1989.

[55] Jiang H. Holton K. Robb R. *Image registration of multimodality 3-D medical images by chamfer matching.* In: Proc SPIE vol 1660 Biomedical Image Processing and Three-Dimensional Microscopy. SPIE Press. Bellingham. WA. pp 356-366. 1992.

[56] Jiang H. Robb RA. Holton KS. *New approach to 3-D registration of multimodality medical images by surface matching.* In Visualisation in Biomedical Computing. Proc SPIE 1808:196-213. 1992.

[57] van den Elsen PA. Maintz JB. Pol ED. Viergever MA. *Image fusion using geometrical features. in Visualisation in Biomedical Computing.* Proc SPIE 1808:172-186 1992.

[58] Hill DLG and Hawkes DJ. *Medical image registration using knowledge of adjency of anatoical structures.* Image and Vision Computing. 12. 173-178 1994.

[59] Collins DL. Dai W. Peters TM. Evans AC. *Model based segmentation of individual brain structures from MRI data.* Visualization in biomedical computing. Proc SPIE 1808:10-23. 1992.

[60] Collins DL. Peters TM. Evans. *Non-linear multi-scal image registration and segmentation of individual brain structures from MRI.* In: Roux C. Herman G.

Colloree R (eds): Proceedings of IEEE Symposium on Advanced Medical Image Processing in Medicine. Rennes. France: IEEE Engineering in Medicine and Biology Society. pp. 105-110. 1992.

[61] Collins DL. Neelin P. Peters TM. Evans AC. *Automatic 3D Intersubject Registration of MR Volumetric Data in Standarized Talairach Space.* Journal of Computer Assisted Tomography 18(20:192-205. March/April. 1994.

[62] Evans AC.Collins DL. Milner B. *An MRI-based stereotactic atlas from 250 young normal subjects.* Soc Neurosci Abstr 1992: 18:408.

[63] Woods RP . Mazziotta JC. Cherry SR. *MRI-PET registration with automated algorithm.* Journal of Computer Assisted Tomography 17:536-646 1993.

[64] Hill DLG. Studholme C. Hawkes D.J. *Voxel similarity measures for automated image registration.* Visualization in Biomedical Computing. SPIE 2359. pp205-216. 1994.

[65] Studholme C. Hill DLG. Hawkes D.J. *Multiresolution voxel similarity measures for MR-PET registration.* In Information Processing in Medical Imagin. Y. Bizais et. al. (eds.). pp. 287-298. 1995.

[66] Eberl S. Kanno I. Fulton RR. et al. *Automatic 3D spatial alignment for correcting inter-study patient motion in serial PET studies.* In Uemura K. Lassen NA. Jones T. Kanno I eds. Quantification of brain function: tracer kinetics and image analysis in PET. pp419-428. 1993.

[67] Hoh CK. Dahlbom M. Harris G. et al. *Automated iterative three-dimensional registration of positron emission tomography images.* J Nucl Med. 34:2009-20018. 1993.

[68] Gerlot-Chiron P. Bizais Y. *Registration of Multimodality medical images using a region overlap criterion.* CVGIP - Graphical Models & Image Processing. v. 54. p. 396-406. Sep.. 1992.

[69] Collignon A. Vandermeulen D. Suetens P. Marchal G. *3D Multi-Modality Medical Image Registration Using Feature Space Clustering.* In Computer Vision. Virtual Reality and Robotics in Medicine. CVRMed'95. N. Ayache (eds.) pp. 195-204. 1995.

[70] Collignon A. Maes F. Delaere D. Vandermeulen D. Suetens P. Marchal G. *Automated multimodality image registration based on information theory.* In Information Processing in Medical Imagin. Y. Bizais et. al. (eds.). pp. 263-274. 1995.

[71] Cover TM. Thomas JA. **Elements of Information Theory.** John Wiley & Sons Inc. New York. 1991.

[72] Duda RO. Hart PE. **Pattern Classification and Scene Analysis.** Standford Research Institute. Melo Park. CA USA. A Wiley-Interscience Publication. 1973.

[73] tar Haar Romeny B. Florack LMJ. Koenderink JJ. Viergever MA. *Scale Space: its natural operators and differential invariants* In: Colchester ACF. Hawkes DJ. eds. Information processing in medical imaging. Wye. UK: Spring-Verlag. 1991:239-255.

[74] Burt PJ. *Fast filter transforms for image processing.* Computer Vision. Graphics. and Image Processing. Vol 16. pp. 20-51. 1981.

[75] Crowley JL. *A Representation for Visual Information.* PhD thesis. Carnegie-Mellon University. Robotics Institute. Pittsburgh. Pennsylvania. 1981.

[76] Parker JA. Kenyon R. and Troxel DE. *Comparison of Interpolating Methods for Image Resampling* IEEE Transactions on Medical Imaging. Vol. MI-2. No. 1. pp. 31-39, 1983.

[77] Neelin P. Crossman J. Hawkes D.J. Ma Y. Evans AC. *Validation of an MRI/PET landmark registration method using 3D simulated PET images and point simulations.* Computerized Medical Imaging and Graphics. Vol 17. No. 4/5 pp. 351-356. 1993.

[78] Kirkpatrick S. Gelatt CD. Vecchi MP. *Optimization by Simulated Annealing.* Science. V. 220. No. 4598. pp. 671 - 680. 1983.

[79] Goldberg DE. **Genetic algorithms in search optimisation and machinve learning.** Addison Welsley. Mass. USA. 1989.

[80] Press WH. Teukolsky SA. Vetterling WT. Flannery BP. **Numeric Recipes in C** (2nd ed.) Cambridge University Press. 1992.

[81] Hill DLG. *Combination of 3D medical images from multiple modalities.* PH.D. thesis of Univerisy of London. 1993.

[82] Brent RP. **Algorithms for Minimization Without Derivatives.** Prentice-Hall, Inc. Englewood Cliffs. New Jersey. 1973.

[83] Schwefel H-P. **Numerical Optimization of Computer Models.** John Wiley & Sons, Ltd., 1981.

[84] van den Elsen PA. Maintz JBA. Pol EJD. Viergver MA. *Automatic Registration of CT and MR Brain Images using Correlation of Geometrical Features.* IEEE Transactions on Medical Imaging. V14:384-396. June. 1995.

[85] Strother SC. Anderson JR. Xu X-L. Liow J-S. Bonar DC. Rottenberg DA. *Quantitative Comparisons of Image Registration Techniques Based on High-Resolution MRI of the Brain* Journal of Computer Assisted Tomography 18(6):954-962. Nov/Dec. 1994.

[86] Kamber M. Shinghal R. Collins DL. Francis GS. Evans AC. *Model-based 3D segmentation of multiple sclerosis lesions in magnetic resonance brain images* IEEE Trans Med Imag 14(3): 442-453. 1995.

[87] Zijdenbos A. Evans AC. Riahi F. Sled J. Chui J. Kollokian V. *Automatic quantification of multiple sclerosis lesion volume using stereotaxic space.* 4th International Conference on Visualization in Biomedical Computing. VBC '96: Hamburg.

[88] Ma Y. Kamber M and Evans AC. *3D Simulation of PET Brain Images Using Segmented MRI Data and Positron Tomograph Characteristics.* Computerized Medical Imaging and Graphics. Vol. 17 Nos. 4/5. pp. 365-371. 1993.

[89] Ma Y, and Evans AC. *A scanner specific sinogram model for PET image reconstruction.* Proc. 17th IEEE-EMBS Annual International Conference. pp. 523-524. Montreal. September 1995.

IMAGE EVALUATION
TEST TARGET (QA-3)

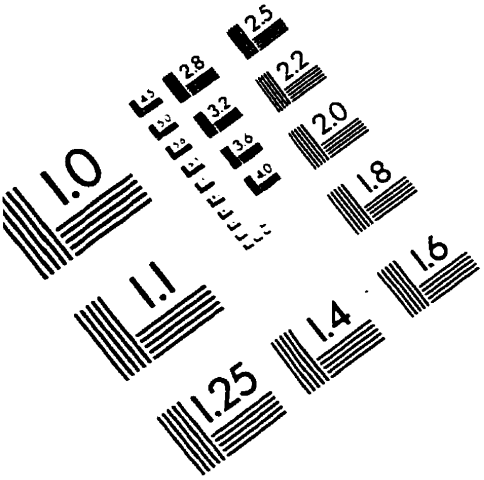

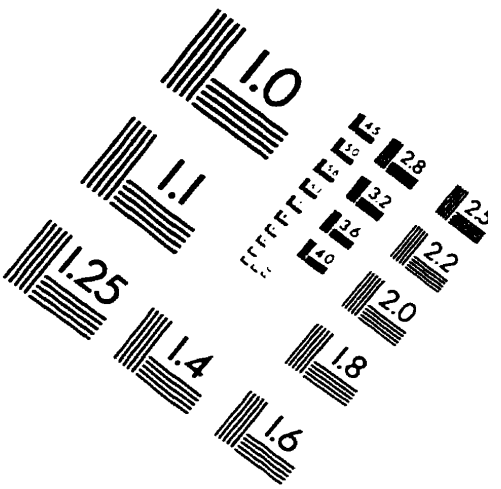

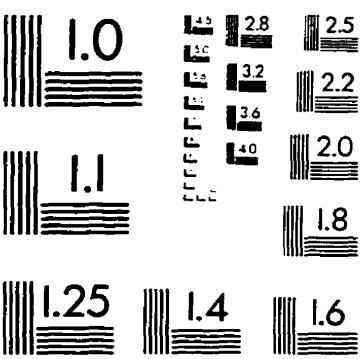

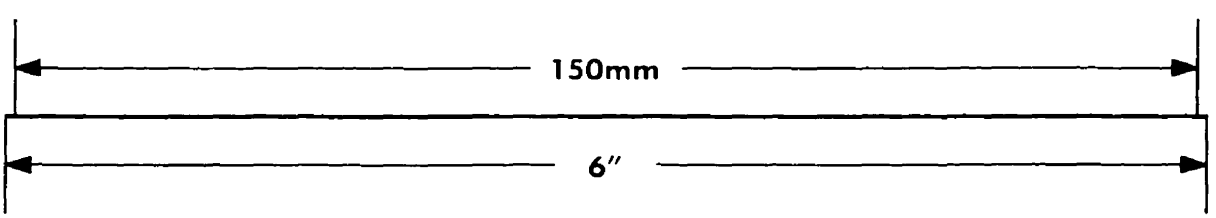

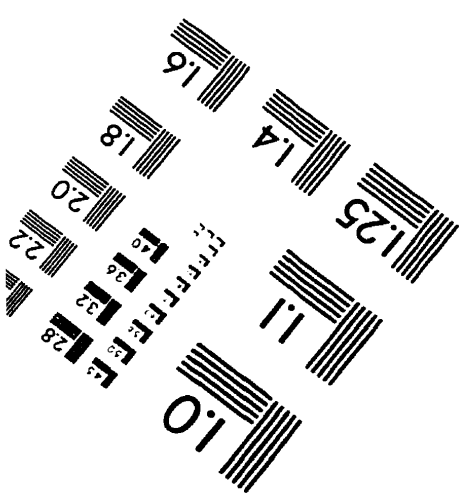

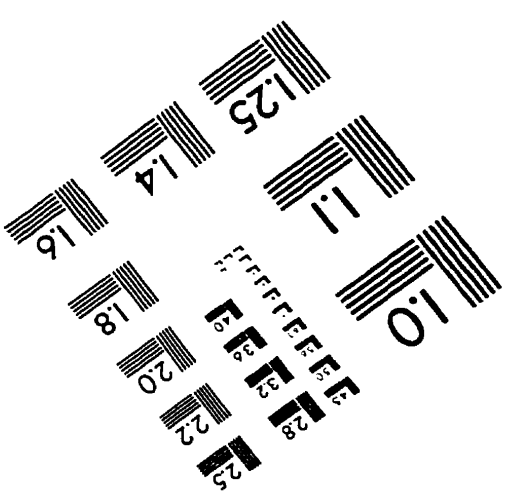

APPLIED IMAGE, Inc
1653 East Main Street
Rochester, NY 14609 USA
Phone: 716/482-0300
Fax: 716/288-5989